

## THE DEEP2 GALAXY REDSHIFT SURVEY: THE GALAXY LUMINOSITY FUNCTION TO $Z \sim 1$

C.N.A. WILLMER<sup>2,3</sup>, S. M. FABER<sup>2</sup>, D. C. KOO<sup>2</sup>, B. J. WEINER<sup>2,4</sup>, J. A. NEWMAN<sup>5,6</sup>, A. L. COIL<sup>7</sup>, A. J. CONNOLLY<sup>8</sup>, C. CONROY<sup>7</sup>, M. C. COOPER<sup>7</sup>, M. DAVIS<sup>7,9</sup>, D. P. FINKBEINER<sup>10</sup>, B. F. GERKE<sup>9</sup>, P. GUHATHAKURTA<sup>2</sup>, J. HARKER<sup>2</sup>, N. KAISER<sup>11</sup>, S. KASSIN<sup>2</sup>, N. P. KONIDARIS<sup>2</sup>, L. LIN<sup>2,12</sup>, G. LUPPINO<sup>11</sup>, D. S. MADGWICK<sup>5,6</sup>, K. G. NOESKE<sup>2</sup>, A. C. PHILLIPS<sup>2</sup>, R. YAN<sup>7</sup>.

*Draft version October 15, 2018*

### ABSTRACT

The evolution of the  $B$ -band galaxy luminosity function is measured using a sample of more than 11,000 galaxies with spectroscopic redshifts from the DEEP2 Redshift Survey. The rest-frame  $M_B$  versus  $U - B$  color-magnitude diagram of DEEP2 galaxies shows that the color-magnitude bimodality seen in galaxies locally is still present at redshifts  $z > 1$ . Dividing the sample at the trough of this color bimodality into predominantly red and blue galaxies, we find that the luminosity function of each galaxy color type evolves differently. Blue counts tend to shift to brighter magnitudes at constant number density, while the red counts remain largely constant at a fixed absolute magnitude. Using Schechter functions with fixed faint-end slopes we find that  $M_B^*$  for blue galaxies brightens by  $\sim 1.3 \pm 0.14$  magnitudes per unit redshift, with no significant evolution in number density. For red galaxies  $M_B^*$  brightens somewhat less with redshift, while the formal value of  $\phi^*$  declines. When the population of blue galaxies is subdivided into two halves using the rest-frame color as the criterion, the measured evolution of both blue subpopulations is very similar.

*Subject headings:* Galaxies: distances and redshifts – galaxies: luminosity function – galaxies: evolution

### 1. INTRODUCTION

The luminosity function is an important tool to analyze redshift surveys since it provides a direct estimate of how much light is contained in galaxies. By characterizing the observed changes with redshift in the luminosity function of galaxies as a function of (rest-frame) wavelength, it is possible to measure how the star-formation rates (e.g., using ultra-violet data) and stellar masses (e.g., using  $K$ -band data) have changed as a function of time. These analyses quantify the observed changes undergone by the galaxies' masses and mass-to-light ratios, thus providing valuable data for theories of galaxy formation.

<sup>1</sup> Based on observations taken at the W. M. Keck Observatory which is operated jointly by the University of California and the California Institute of Technology

<sup>2</sup> UCO/Lick Observatory, University of California, 1156 High Street, Santa Cruz, CA, 95064, [cnaw@ucolick.org](mailto:cnaw@ucolick.org), [faber@ucolick.org](mailto:faber@ucolick.org), [koo@ucolick.org](mailto:koo@ucolick.org), [bjw@ucolick.org](mailto:bjw@ucolick.org), [raja@ucolick.org](mailto:raja@ucolick.org), [jharker@ucolick.org](mailto:jharker@ucolick.org), [kassin@ucolick.org](mailto:kassin@ucolick.org), [npk@ucolick.org](mailto:npk@ucolick.org), [lihwai@ucolick.org](mailto:lihwai@ucolick.org), [kai@ucolick.org](mailto:kai@ucolick.org), [phillips@ucolick.org](mailto:phillips@ucolick.org)

<sup>3</sup> On leave from Observatório Nacional, Rio de Janeiro, Brazil

<sup>4</sup> Present address: Department of Astronomy, University of Maryland, College Park, MD 20742

<sup>5</sup> Lawrence Berkeley Laboratory, Berkeley, CA 94720, [janewman@lbl.gov](mailto:janewman@lbl.gov)

<sup>6</sup> Hubble Fellow

<sup>7</sup> Department of Astronomy, University of California, 601 Campbell, Berkeley, CA 94720, [acoil@astron.berkeley.edu](mailto:acoil@astron.berkeley.edu), [cconroy@astron.berkeley.edu](mailto:cconroy@astron.berkeley.edu), [cooper@astron.berkeley.edu](mailto:cooper@astron.berkeley.edu), [mdavis@astron.berkeley.edu](mailto:mdavis@astron.berkeley.edu), [renbin@astron.berkeley.edu](mailto:renbin@astron.berkeley.edu)

<sup>8</sup> Department of Physics and Astronomy, University of Pittsburgh, Pittsburgh, PA 15260, [ajc@phyast.pitt.edu](mailto:ajc@phyast.pitt.edu)

<sup>9</sup> Department of Physics, Le Conte Hall, UC-Berkeley, Berkeley, CA 94720, [bgerke@astro.Berkeley.EDU](mailto:bgerke@astro.Berkeley.EDU)

<sup>10</sup> Department of Astrophysics, Princeton University, Peyton Hall, Princeton, NJ 08544 [dfink@astro.princeton.edu](mailto:dfink@astro.princeton.edu)

<sup>11</sup> Institute for Astronomy, 2680 Woodlawn Drive Honolulu, HI, 96822-1897, [kaiser@ifa.hawaii.edu](mailto:kaiser@ifa.hawaii.edu), [ger@ifa.hawaii.edu](mailto:ger@ifa.hawaii.edu)

<sup>12</sup> Department of Physics, National Taiwan University, No. 1, Sec.4, Roosevelt Road, Taipei 106, Taiwan

The measurement of the galaxy luminosity function for samples of field galaxies (i.e., galaxies selected for redshift measurements independent of their local environment) has been made for almost every major redshift survey (see Binggeli et al. 1998, Tresse 1999 and de Lapparent et al. 2003 for reviews). Thanks to major surveys such as the Two-Degree Field Galaxy Redshift Survey (Colless et al. 2001) and the Sloan Digital Sky Survey (York et al. 2000), precise measurements of the luminosity function in the local ( $z < 0.3$ ) universe are available (e.g., Norberg et al. 2002; Blanton et al. 2003; Bell et al. 2003), providing a benchmark to measure the luminosity function evolution.

The characterization of properties of galaxies at redshifts  $z \sim 1$ , a time when the universe was half its present age, is then an important step to fully understand how galaxies formed and evolve. The DEEP2 Redshift Survey (Davis et al. 2003) is a project that is measuring 50,000 galaxy redshifts in four widely separated regions of the sky, comprising a total area of  $3.5 \square^\circ$ , and is specifically designed to probe the properties of galaxies at redshifts beyond  $z = 0.7$ .

In a series of two papers, the  $B$ -band galaxy luminosity function to  $z \sim 1$  will be investigated using the DEEP2 Redshift Survey (this paper), followed by an analysis that combines DEEP2 with other major current surveys of distant galaxies (Wolf et al. 2003; Gabasch et al. 2004; Ilbert et al. 2005), discussing possible evolutionary scenarios for early and late type galaxies (Faber et al. 2005, hereafter Paper II). The choice of  $B$ -band rather than other rest-frame wavelengths is motivated by the large number of measurements in this spectral range both for local as well as for distant samples of galaxies. An additional advantage is that for most of the higher-redshift intervals considered in this work, observed  $R$  and  $I$  are sampling rest-frame  $B$ , thus minimizing the importance

of K-corrections. The present paper uses data from  $\sim 1/4$  of the total DEEP2 survey to measure the galaxy luminosity function, and discusses the importance of several selection effects in its measurement. This analysis will also take advantage of the recently found *bimodality* of galaxies in the color-magnitude diagram (Strateva et al. 2001; Hogg et al. 2003; Baldry et al. 2004 and references therein), where the predominantly red early-type galaxies occupy a distinct locus in color from the blue star-forming galaxies. This bimodality has been shown to extend to  $z \sim 1$  (Im et al. 2002; Bell et al. 2004; Weiner et al. 2005) and beyond (e.g., Giallongo et al. 2005). A bimodal distribution is also seen for other parameters such as spectral class (Madgwick et al. 2002, 2003), morphologies, metallicities, and star formation rates (Kauffmann et al. 2003). The present paper will show that this bimodality persists to  $z \sim 1$ , and that it is related on how these two populations have evolved over the last 6 Gyr.

This paper is organized as follows: §2 presents the DEEP2 data used in this paper, describing the selection effects that are present in this sample; §3 describes the methods used to measure the luminosity function and its evolution, and the weighting scheme that was adopted to correct for the incomplete data sampling; §4 presents the analysis of DEEP2 data showing how the evolution of the galaxy luminosity function depends on the internal properties of galaxies, blue galaxies showing mainly luminosity evolution while the red galaxy luminosity function shows a decrease in number density toward higher redshifts. Two appendices follow, describing the method used to calculate the K-corrections and another estimating biases in the luminosity function calculation by making cuts at different limiting absolute magnitudes. Throughout this work, a  $(H_0, \Omega_M, \Omega_\Lambda) = (70, 0.3, 0.7)$  cosmology is used. Unless indicated otherwise, magnitudes and colors are converted into the Vega system, following the relations shown in Table 1.

## 2. DATA

This section gives a brief description of the DEEP2 data; for more details the reader is referred to Davis et al. (2003), who give an outline of the project, Faber et al. (in preparation), who describe the survey strategy and spectroscopic observations, Coil et al. (2004b), who describe the preparation of the source catalog, and Newman et al. (in preparation), where the spectroscopic reduction pipeline is described.

The photometric catalog for DEEP2 (Coil et al. 2004b) is derived from Canada-France-Hawaii Telescope (CFHT) images taken with the  $12K \times 8K$  mosaic camera (Cuillandre et al. 2001) in  $B$ ,  $R$  and  $I$  in four different regions of the sky. The  $R$ -band images have the highest signal-to-noise and were used to define the galaxy sample, which has a limiting magnitude for image detection at  $R_{AB} \sim 25.5$ . Objects were identified using the *imcat* software written by N. Kaiser and described by Kaiser, Squires & Broadhurst (1995). In addition to magnitudes, *imcat* calculates other image parameters which are used in the object classification. The separation between stars and galaxies is based on magnitudes, sizes, and colors, which are used to assign each object a probability of being a galaxy ( $P_{gal}$ ). For the DEEP2 fields, the cut is made at  $P_{gal} > 0.2$ , *i.e.*, objects are con-

sidered as part of the sample whenever the probability of being a galaxy is greater than 20%. In Fields 2, 3, and 4, the spectroscopic sample is pre-selected using  $B$ ,  $R$ , and  $I$  to have estimated redshifts greater than 0.7, which approximately doubles the efficiency of the survey for galaxies near  $z \sim 1$ . The fourth field, the Extended Groth Strip (EGS), does not have this pre-selection but instead has roughly equal numbers of galaxies below and above  $z = 0.7$  selected using a well understood algorithm. In addition to the redshift pre-selection, a surface brightness cut defined as

$$SB = R_{AB} + 2.5 \text{Log}_{10}\{\pi(3r_g)^2\} \leq 26.5, \quad (1)$$

is applied when selecting spectroscopic candidates, where  $R_{AB}$  is the  $R$ -band (AB) magnitude, and  $r_g$  is the  $1 \sigma$  radius of the Gaussian fit to the image profile in the CFHT photometry; the minimum size for  $r_g$  is fixed at  $0''.33$ , so that for compact objects with  $3r_g < 1''$ , the surface brightness is measured within a circular aperture of  $1''$ . Finally, galaxies were selected to lie within bright and faint apparent-magnitude cuts of  $18.5 \leq R_{AB} \leq 24.1$ .

The DEEP2 sample used here combines data from the first season of observations in Fields 2, 3, and 4 with about  $1/4$  of the total EGS data, which provides an initial sample at low redshifts. The total number of galaxies is 11284, with 4946 (45%) in EGS, 3948 (36%) in Field 4, 2299 (21%) in Field 3, and 91 (1%) in Field 2. Because of the  $BRI$  redshift pre-selection, for  $z < 0.8$ , only EGS is sampled well enough to be used, while data in all four fields are used for  $z \geq 0.8$ .

DEEP2 spectra were acquired with the DEIMOS spectrograph (Faber et al. 2003) on the Keck 2 telescope and processed by an automated pipeline that does the standard image reduction (division by flatfield, rectification of spectra, extraction of 2-D and 1-D spectra) and redshift determination (Newman et al., in preparation). The only human intervention occurs during redshift validation, where spectra and redshifts are visually examined, and redshifts are given a quality assessment that ranges from 1 (for completely indeterminate) to 4 (for ironclad). Only redshifts with quality 3 and 4 are used in this paper, which means that two or more features have been identified (the [O II]  $\lambda 3727$  doublet counts as two features). Duplicate observations and other tests indicate an rms accuracy of  $30 \text{ km s}^{-1}$  and an unrecoverable failure rate of  $\sim 1\%$  for this sample.

The apparent color-magnitude (CM) diagram in  $R$  versus  $R-I$  is shown in Figure 1a for the DEEP2 parent catalog after applying the photometric-redshift cut in three of the fields and converting into Vega magnitudes (cf. Table 1). Figure 1b shows the distribution of galaxies placed on masks, Figure 1c shows galaxies with successful redshifts, and Figure 1d shows galaxies with “failed” redshifts. Although failures are found in all parts of the diagram, the largest concentration is at faint and blue magnitudes. Independent data show that the great majority of these are beyond  $z \sim 1.4$  (C. Steidel, private communication), corresponding to [O II]  $\lambda 3727$  passing beyond the DEEP2 wavelength window at that redshift. Redshift histograms corresponding to the rectangular regions outlined in Figure 1 are shown in Figure 2, where the vertical bars at the right of each diagram represent the number of failed redshifts in each bin. The increase in failures for faint and blue galaxies is apparent.

Figure 3a plots  $U - B$  versus distance for the whole sample, where the rest-frame color is calculated using the K-correction procedure described in Appendix A. Throughout this paper, the rest-frame colors and magnitudes are corrected for Galactic extinction (Schlegel, Finkbeiner & Davis 1998) but not internal extinction. Color bimodality dividing red and blue galaxies is immediately apparent, extending to beyond  $z = 1$ . Panel *b* shows the EGS by itself, while panels *c* and *d* show the high effectiveness of the *BRI* photometric selection in Fields 2, 3, and 4.

Figure 4 plots CM diagrams using  $U - B$  versus  $M_B$  as a function of redshift. The solid line in each panel represents the limiting absolute magnitude at the high redshift end of each bin. The slope of this line changes with redshift because of the adoption of a fixed apparent magnitude limit ( $R$ ) for the sample, with the color-redshift-dependence of the K-correction. At  $z \sim 0.4$  the  $R$ -band filter used to select the sample coincides with rest  $B$  but differs from it increasingly as the redshift is either greater or smaller than 0.4.

The bimodality in color-magnitude distribution is clearly seen; while red galaxies tend to be brighter on average than blue galaxies, it is clearly seen that blue galaxies dominate the sample when number of objects is considered. The upper dashed lines represent the cut used to separate red and blue galaxies, as explained in §4.1. Since the evidence of color evolution in DEEP2 data is slight, the zero-point and slope of this line with redshift is kept constant. The lower dashed lines have the same slope and are used to divide blue galaxies into two equal halves for further luminosity-function analysis; their zero-points are explained in §4.2.

An interesting feature of these diagrams is that, even though the detection of faint galaxies is favored at low redshifts, there are still very few red galaxies found with  $M_B > -18$ , even at redshifts below  $z \sim 0.6$ , where they should be seen. The same absence was also seen by Weiner et al. (2005) in DEEP1 and by Kodama et al. (2004) in distant clusters. This point is discussed further in the context of COMBO-17 data in Paper II.

### 3. METHODS

#### 3.1. Luminosity Function Estimators

The luminosity function is defined as the number of galaxies per unit magnitude bin per unit co-moving volume, and is most frequently expressed using the Schechter (1976) parameterization, which in magnitudes is:

$$\phi(M)dM = 0.4 \ln 10 \phi^* 10^{0.4(M^* - M)(\alpha + 1)} \times \exp\{-10^{0.4(M^* - M)}\} dM, \quad (2)$$

where  $\phi^*$  represents the characteristic number density of galaxies per unit volume per unit magnitude,  $M^*$  the characteristic magnitude where the growth of the luminosity function changes from an exponential into a power law, and  $\alpha$  the slope of this power law that describes the behavior of the faint end of this relation. Several estimators have been proposed to measure this statistic (e.g., Schmidt 1968; Lynden-Bell 1971; Turner 1979; Sandage, Tammann & Yahil 1979; Choloniewski 1986; Efstathiou, Ellis & Peterson 1988), and the relative merits of the different methods were explored by Willmer (1997) and

Takeuchi, Yoshikawa & Ishii (2000) through the use of Monte-Carlo simulations.

In this work, the luminosity function calculation relies on two estimators. The first is the intuitive  $1/V_{max}$  method where galaxies are counted within a volume. The calculation used here follows Eales (1993), Lilly et al. (1995), Ellis et al. (1996) and Takeuchi et al. (2000), which overcomes the bias identified by Felten (1976) and Willmer (1997). The integral luminosity function for an absolute magnitude bin between  $M_{bright}$  and  $M_{faint}$  is described as:

$$\int_{M_{bright}}^{M_{faint}} \phi(M) dM = \sum_{i=1}^{N_g} \frac{\chi_i}{V_{max}(i)}, \quad (3)$$

where  $\chi_i$  is the galaxy weight that corrects for the sampling strategy used in the survey (discussed in detail in §3.3 below) and  $V_{max}(i)$  is the maximum co-moving volume within which a galaxy  $i$  with absolute magnitude  $M_i$  may be detected in the survey:

$$V_{max}(i) = \int_{\Omega} \int_{z_{min,i}}^{z_{max,i}} \frac{d^2V}{d\Omega dz} dz d\Omega, \quad (4)$$

where  $z$  is the redshift and  $\Omega$  the solid angle being probed. In a survey that is limited at bright ( $m_l$ ) and faint ( $m_u$ ) apparent magnitudes, the redshift limits  $z_{min,i}$  and  $z_{max,i}$  for galaxy  $i$  are:

$$z_{max,i} = \min\{z_{max}, z(M_i, m_u)\} \quad (5)$$

$$z_{min,i} = \max\{z_{min}, z(M_i, m_l)\} \quad (6)$$

where the terms in braces are the redshift limits imposed either by the limits of the redshift bin being considered ( $z_{min}$  and  $z_{max}$ ) or by the apparent magnitude limits of the sample ( $m_l$  and  $m_u$ ). The Poisson error for the  $1/V_{max}$  method in a given redshift bin is given by:

$$\sigma_{\phi} = \sqrt{\frac{\chi_i}{(V_{max}(i))^2}}. \quad (7)$$

In this paper, the  $1/V_{max}$  method is calculated in absolute magnitude bins 0.5 mag wide, and redshift bins of width  $\Delta z = 0.2$ . The result is the average value of the luminosity function  $\phi(M_k, z)$  at redshift  $z$  in magnitude bin  $k$ . The method makes no assumption about the shape of the luminosity function, therefore providing a non-parametric description of the data.

The second estimator is the most commonly used in luminosity function calculations – the parametric maximum-likelihood method of Sandage, Tammann and Yahil (1979, STY; Efstathiou, Ellis & Peterson 1988; Marzke, Huchra & Geller 1994). The STY method fits an analytic Schechter function (Equation 2), yielding values of the shape parameters  $M^*$  and  $\alpha$  (but not the density normalization  $\phi^*$ ).

The probability density that a galaxy with absolute magnitude  $M_i$  will be found in a redshift survey sample is proportional to the ratio between the differential luminosity function at  $M_i$  and the luminosity function integrated over the absolute magnitude range that is detectable at redshift  $z_i$ . In the case of DEEP2 galaxies, the STY conditional probabilities were modified following Zucca, Pozzetti, & Zamorani (1994) to account for the galaxy weights,  $\chi_i \geq 1$  (see §3.3 below), correcting for

the sampling (e.g., Lin et al. 1999) and redshift success rates:

$$p(M_i, z_i) = \left[ \frac{\phi(M_i)dM}{\int_{M_{bright(z_i)}}^{M_{faint(z_i)}} \phi(M)dM} \right]^{\chi_i}. \quad (8)$$

Here  $M_{bright(z_i)}$  and  $M_{faint(z_i)}$  are the absolute magnitude limits at redshift  $z_i$  accessible to a sample with apparent magnitude limits  $m_u$  and  $m_l$ .  $M_{bright(z_i)}$  and  $M_{faint(z_i)}$  are implicitly a function of color (cf. Figure 4), which motivates the approach (used here) to divide galaxies at least broadly into two color bins. Implicitly,  $\phi(M)$  is assumed to vary with  $z$ ; the analysis is carried out in fixed redshift bins in which  $\phi(M, z)$  is determined.

The likelihood function maximized by the STY method is defined by the joint probability of all galaxies in the sample belonging to the same parent distribution. The solution is obtained by assuming a parametric form for the luminosity function and maximizing the logarithm of the likelihood function relative to the product of the probability densities of the individual galaxies  $p(M_i, z_i)$ :

$$\ln \mathcal{L} = \ln \prod_{i=1}^{N_g} p(M_i, z_i). \quad (9)$$

Because this method uses no type of binning, it preserves all information contained in the sample. Since the luminosity function normalization is canceled out (Equation 8), it is insensitive to density fluctuations in the galaxy sample. However, this also means that the normalization (defined by  $\phi^*$ ) must be estimated separately, using the procedure described in §3.2 below.

Another shortcoming of the STY method is that it does not produce a visual check of the fit. However, this can be done using the  $1/V_{max}$  method, which shows the average number density of galaxies in bins of absolute magnitude and can be compared directly to the shape parameters of the STY results. The  $1/V_{max}$  points also provide an independent check on the luminosity function normalization.

### 3.2. Luminosity Function Normalization

Since the STY probability estimator is defined from the ratio between the differential and integral luminosity functions, the density normalization is factored out and has to be estimated independently. The standard procedure for obtaining the luminosity function normalization ( $\phi^*$ ) measures the mean number density of galaxies in the sample,  $\bar{n}$ , which is then scaled by the integral of the luminosity function:

$$\phi^* = \frac{\bar{n}}{\int_{M_{bright}}^{M_{faint}} \phi(M)dM} \quad (10)$$

where  $M_{bright}$  and  $M_{faint}$  are the brightest and faintest absolute magnitudes considered in the survey.

The method used to measure the mean density  $\bar{n}$  is the unbiased minimum-variance estimator proposed by Davis & Huchra (1982):

$$\bar{n} = \frac{\sum_{i=1}^{N_g} \chi_i N_i(z_i) w(z_i)}{\int_{z_{min}}^{z_{max}} s(z) w(z) \frac{dV}{dz} dz}, \quad (11)$$

which averages the redshift distribution of galaxies,  $N_i(z_i)$ , corrected by a weighting function,  $w(z_i)$ , that takes into account galaxy clustering; the selection function,  $s(z)$ , that corrects for the unobserved portion of the luminosity function; and the sampling weight,  $\chi_i$ . The selection function is given by:

$$s(z) = \frac{\int_{max(M_{min(z_i)}, M_{bright})}^{min(M_{max(z_i)}, M_{faint})} \phi(M)dM}{\int_{M_{bright}}^{M_{faint}} \phi(M)dM}. \quad (12)$$

where  $M_{min(z_i)}$  and  $M_{max(z_i)}$  are the brightest and faintest absolute magnitudes at redshift  $z_i$  contained within the apparent magnitude limits of the sample. The contribution due to galaxy clustering is accounted for by the second moment  $J_3$  of the two-point correlation function  $\xi(r)$  (e.g., Davis & Huchra 1982), which represents the mean number of galaxies in excess of random around each galaxy out to a distance  $r$  (typically set at  $\sim 30$  Mpc):

$$w(z_i) = \frac{1}{1 + \bar{n} J_3 s(z)}, \quad J_3 = \int_0^r r^2 \xi(r) dr. \quad (13)$$

Because of the small range of absolute magnitudes available at high redshift, the shape of the faint end slope, parameterized by  $\alpha$  is not constrained by the fit, so we opted to keep the value of this parameter fixed, as discussed in §4.2. Thus, in the calculation of errors for the Schechter parameters only  $M^*$  and  $\phi^*$  are considered. Since the STY method factors out the density, it is also not suitable for calculating the correlated errors of  $\phi^*$  and  $M^*$ , as, lacking  $\phi^*$ , STY cannot take the high correlation between these two errors into account. These errors were therefore calculated from the  $1-\sigma$  error ellipsoid (Press et al. 1992) that resulted from fitting the Schechter function to the  $1/V_{max}$  data points. Although the luminosity functions that result from the STY and  $1/V_{max}$  methods are not quite identical (cf. Figure 7), the differences are small, and errors from  $1/V_{max}$  should also be applicable to the STY method.

### 3.3. The Sampling Function and Galaxy Weights

An issue with every data set is the selection of weights to correct for missing galaxies. The adopted weights need to take into account the fact that (1) objects may be missing from the photometric catalog, (2) stars may be identified as galaxies and vice versa, (3) not all objects in the photometric catalog are targeted for redshifts (sampling rate) and (4) not all redshift targets yield successful redshifts (redshift success rate). In the case of DEEP2, since the limiting magnitude of the photometric catalog is 1.5 magnitudes fainter than the limit adopted for redshift selection, any effects due to incompleteness of the source catalog should be negligible. The loss of galaxies brighter than  $R_{AB}=24.1$  but with surface brightness too low to admit them in the photometric catalog is ruled out from the inspection of HST images analyzed by Simard et al. (2002) for the EGS region in common with Groth Strip, which shows no large low-surface brightness galaxies. The loss of galaxies because of confusion with stars in well-defined regions of the color-magnitude diagram (item 2 above) is shown in §3.4 below to be negligible. Therefore, only factors (3) and (4) need to be taken into account in the weights. The basic assumption to deal

with (3) is that all unobserved galaxies share the same average properties as the observed ones in a given color-magnitude bin. The last effect, factor (4), is dealt with by assigning a model redshift distribution to the failed galaxies.

A visual description of how the sampling rate and redshift success rates depend on the magnitude and color of galaxies is shown in Figure 5, which projects both rates averaged in a color-color-magnitude data cube onto the  $R$  versus  $R - I$  plane. Both rates are shown separately for EGS and Fields 2-4 because of the different selection criteria. In the EGS, the average sampling rate of slits placed on galaxies is  $\sim 60\%$ , and the average redshift success is  $73\%$ . For Fields 2, 3, and 4, the average sampling rate is  $59\%$  (after foreground galaxies are eliminated via color pre-selection), and the redshift success is  $73\%$ .

To account for the unobserved galaxies and redshift failures we follow in this paper (and in Paper II for DEEP1 data) the method first applied by Lin et al. (1999) to the CNOC2 Redshift Survey. This defines around each galaxy  $i$  a data cube in color-color-magnitude space and, from all attempted redshifts, counts the number of failed redshifts ( $N_f$ ), the number ( $N_{z_h}$ ) of galaxies with  $z > z_h$ , where  $z_h$  is the high redshift limit of the sample; the number ( $N_{z_l}$ ) of galaxies with  $z < z_l$ , where  $z_l$  is the low redshift limit of the sample and the number ( $N_z$ ) with good redshifts within the “legal” redshift range  $z_l$  to  $z_h$ . For Fields 2-4,  $z_l = 0.8$  and  $z_h = 1.4$ ; and for EGS these are  $z_l = 0.2$  and  $z_h = 1.4$ .

Next, for each galaxy in the photometric source catalog, the probability that it has a redshift in the legal redshift range is estimated. In the case of galaxies with good-quality redshifts, the probability that the redshift lies in the legal range is simply  $P(z_l \leq z \leq z_h) = 1$  when the galaxy has  $z_l \leq z \leq z_h$  and  $P(z_l \leq z \leq z_h) = 0$  for  $z > z_h$  or  $z < z_l$ . To get the probability for unobserved galaxies, however, some assumption must be made for the distribution of the *failed* redshifts. Two main models are used in the present work. The first assumes that all failed redshifts are beyond the high redshift cutoff of the sample,  $z_h$  (the “minimal” model). In this case, the probability that an unobserved galaxy will be within the legal redshift range is the ratio of the number of good redshifts in the range divided by the sum of the number of successful redshifts plus failures:

$$P(z_l \leq z \leq z_h) = \frac{N_z}{N_z + N_{z_l} + N_{z_h} + N_f}. \quad (14)$$

The alternative model assumes that failures follow the same distribution as the observed sample (the “average” model). In this case, Equation 15 becomes:

$$P(z_l \leq z \leq z_h) = \frac{N_z}{N_z + N_{z_l} + N_{z_h}}. \quad (15)$$

Finally, the weight for each galaxy  $i$  with an acceptable redshift is calculated by adding for all galaxies  $j$  within the color-color-magnitude bin the probability that the redshift of galaxy  $j$  is within the legal limits of the sample

$$\chi_i = \frac{\sum_j P(z_l \leq z_j \leq z_h)}{N_z}, \quad (16)$$

where  $j$  includes both galaxies with and without attempted redshifts.

In the case of EGS, a final correction is applied to the weights to account for the different sampling strategy that was used, which includes low-redshift galaxies but de-weights them so that they do not dominate the sample. This (independently known) correction ( $f_m$ , Faber et al. in preparation; Newman et al. in preparation) depends on the location of the galaxy in  $B - R$  versus  $R - I$  and its apparent magnitude. From this correction, the probability that a galaxy will be placed on an EGS mask is given by:

$$P(\text{mask}) = 0.33 + 0.43 P_{gal} f_m, \quad (17)$$

where  $P_{gal}$  is the probability that an object is a galaxy. For EGS galaxies the final probability weight is given by

$$\chi_i = \frac{\sum_j P(z_{min} \leq z_j \leq z_{max})}{N_z P(\text{mask})}, \quad (18)$$

where  $j$  includes both galaxies with and without redshifts.

The comparison of Equations 14 and 15 shows that weights in the average model are larger than in the minimal model. The weights and differences in weights between the minimal and average models are shown in Figure 6. These differences are typically of order 15-20% and most large differences occur for galaxies with extreme colors at faint magnitudes.

Based on the unpublished data of Steidel mentioned in §2, the minimal model more closely matches blue galaxies since most failed blue galaxies lie beyond the upper redshift limit of the survey  $z_h=1.4$ . In contrast, most failed red galaxies probably lie within the survey range and are better described by the average model. Because of this behavior, for the All galaxy sample we adopt a compromise “optimal” model, where blue galaxies have weights described by the minimal model, while red galaxies use the average model. However, since the All sample is dominated by blue galaxies, the differences between the optimal and minimal models are very small.

### 3.4. Other Sources of Incompleteness

Several tests were carried out to estimate the impact of what we believe are the principal sources of incompleteness, namely the surface brightness limit for slit assignment, the misclassification of objects, and the presence of dropouts in the  $B$  band photometry.

To limit the rate of redshift failures, a surface brightness cut (Equation 1) was used to place galaxies on slits. This restriction eliminates both red ( $R - I > 1.25$ ) and blue ( $R - I \leq 1.25$ ) galaxies, but the numbers are small. The overall fraction of red galaxies that lie below the surface brightness cut is  $\sim 3\%$ , increasing to  $6\%$  over the faintest  $0.5$  magnitude. For blue galaxies, the average number is  $\sim 5\%$ , increasing to  $7\%$  in the faintest  $0.5$  magnitude bin. In both cases, these numbers are accounted for by the weighting, since all galaxies that were not placed on slits are still counted when the weights are calculated, so no additional corrections are needed, as long as the characteristics of lower-surface brightness galaxies are similar to those of other galaxies situated in the same color-color-magnitude bin.

As mentioned in §2, the star-galaxy separation relies on the colors and sizes of detected objects to assign each one the probability of being a galaxy ( $P_{gal}$ ). Since stars

occupy a well defined locus in the  $R-I$  vs.  $B-R$  diagram (Coil et al. 2004b), it is possible that DEEP2 galaxies with small apparent sizes and observed colors close to the stellar locus could be treated as stars ( $P_{gal} < 0.2$ ) in DEEP2 mask-making and thus be ignored in the analysis since the latter are not placed on masks. This loss is estimated using objects in common between DEEP2 and the structural catalog of Simard et al. (2002), which is derived from psf-corrected photometry using HST images in the original Groth Strip. When plotting the half-light radius *versus* total-magnitude distribution (e.g., Figure 6 of Im et al. 2002), stars and galaxies are well separated down to the limiting magnitude  $R_{AB} = 24.1$  adopted by DEEP2, which corresponds to approximately  $I814 \sim 23.5$ . For red objects located close to the red stellar locus ( $R-I \geq 1.25$ ,  $1.8 \leq B-R \leq 3.5$ ), a total of 8 objects that are clearly galaxies in HST images are identified as stars ( $P_{gal} < 0.2$ ) in the DEEP2 source catalog, while 64 galaxies ( $P_{gal} \geq 0.2$ ) are correctly identified within the same color boundaries. This corresponds to a loss of (8/64) or 13%. On the other hand, the number of spectroscopically observed stars misclassified as (red) galaxies, corresponds to  $\sim 8\%$  of the sample in the faintest magnitude bin ( $23.5 \leq R_{AB} \leq 24.1$ ). An examination of the distribution of surface brightnesses shows that all of these have  $SB \leq 25 R_{AB} \text{ mag arc sec}^{-2}$ , but that there are also galaxies in this range. Thus, the inspection of HST images and the distribution of sizes and surface brightnesses suggests that DEEP2 may be biased against high surface brightness red galaxies with small apparent sizes. However, no strong dependence with redshift was seen. Since the corrections for both effects are very uncertain, we opted not to apply them in the analysis.

A final systematic error is caused by the presence of  $B$ -band dropouts, which are objects that have good  $R$  and  $I$  magnitudes, but a low S/N or non-existent  $B$  measurement. All three magnitudes ( $B, R, I$ ) are needed to sort galaxies from stars; if  $B$  is too dim and noisy, that object is never assigned to a slit. Moreover, as there are no  $B-R$  colors for the dropouts, such objects are also not accounted for in the weighting procedure described above which uses bins in color-color-magnitude space. Consequently, the weights were modified to account for the loss of these objects by counting the number of dropouts within each ( $R, R-I$ ) bin around a given galaxy and dividing this number by the total number of galaxies in the same bin. These corrections are typically less than 4%, though in some bins can reach  $\sim 8\%$ , and are applied to the final weights of each galaxy. The apparent  $R-I$  colors are consistent with most of these objects being part of the red sequence.

In summary, since most of these systematic effects due to incompleteness are small, they will not affect the final conclusions of this paper. Analyses carried out ignoring the last correction produce essentially identical results to those in the present paper.

#### 4. ANALYSIS

##### 4.1. The Non-Parametric Luminosity Functions

The DEEP2 luminosity function is shown in Figure 7, the top row corresponding to the ‘‘All’’ galaxy function, while the second and third rows show the luminosity function determined for sub-samples of galaxies divided into ‘‘Blue’’ and ‘‘Red’’ by using the color bimodality.

The weighting model (§3.3) adopted for each population is identified in the rightmost panel of each row.

For DEEP2 data, the color division between Red and Blue corresponds to the upper dotted line in Figure 4, which is given by:

$$U - B = -0.032(M_B + 21.52) + 0.454 - 0.25. \quad (19)$$

This equation was derived from the van Dokkum et al. (2000) color-magnitude relation for red galaxies in distant clusters, converted to the cosmological model used in this paper and shifted downward by 0.25 mag in order to pass through the valley between red and blue galaxies. Although the colors of red galaxies may evolve with redshift, this effect is not strongly seen in DEEP2 colors, and a line with constant zero-point independent of redshift is adequate for all redshift bins. The constancy of  $U - B$  contrasts with the changes seen in the  $U - V$  vs.  $M_V$  of COMBO-17 (B04). However, when  $U - B$ ,  $U - V$  and  $B - V$  colors are plotted as a function of  $z$  for the COMBO-17 sample, most of the color change can be traced to the  $B - V$  color (C. Wolf, private communication), implying that the stability of the DEEP2 color-magnitude relation over this redshift interval is not inconsistent with B04.

The separation between blue and red galaxies therefore is using a clear feature which is easily identified, even if its physical interpretation is not completely understood (e.g., Kauffmann et al. 2003).

Along the rows of Figure 7, each panel represents a different redshift bin, with  $z$  increasing from left to right. The DEEP2 non-parametric luminosity function estimated using the  $1/V_{max}$  method is represented by the solid black squares. The sample used in the calculation of the luminosity function is shown in Figure 4. The absolute magnitude range is truncated at the faintest absolute magnitude which contains both red and blue galaxies, so that both populations are sampled in an unbiased way. A fully volume-limited sample for a given redshift bin would be obtained using the solid colored lines in Figure 4, which show limiting absolute magnitudes of the upper redshift of each bin, whereas the actually adopted limit (for the purpose of calculation of the luminosity functions), corresponds to the lower redshift limit of the bin. The slight loss of galaxies in the remainder of the bin does not affect the STY estimation since the range of absolute magnitudes accessible at any given  $z$  is calculated on a galaxy-by-galaxy basis. In contrast, the  $1/V_{max}$  method will systematically underestimate the density of galaxies unless corrected, which was done by following Page & Carrera (2000). The error bars represent counting errors assuming Poisson statistics only. The uncertainty due to cosmic variance is shown as a separate error bar at the top left corner of each panel and was estimated following Newman & Davis (2002) who account for evolution of the correlation function using the mass power spectrum, and using the correct field geometry, that takes into account the elongated nature of DEEP2 fields which reduces the cosmic variance. The bias factors derived by Coil et al. (2004a) for red galaxies ( $b = 1.32$ ) and blue galaxies ( $b = 0.93$ ) relative to the mass are included in these cosmic variance estimates. To first order, cosmic variance should affect mainly the overall number density,  $\phi^*$ , moving all points up and down together and leaving the shape of the function unchanged, whereas Poisson vari-

ance is random from point to point; therefore we show the Poisson and cosmic variance error bars separately. The dashed gray curves represent the DEEP2 luminosity function fits (§4.2) measured in the lowest redshift bin ( $0.2 \leq z < 0.4$ ), which are repeated in subsequent panels. The major conclusions are as follows:

*All galaxies (top row):* Relative to the low- $z$  Schechter function, the data in successive redshift bins march to brighter magnitudes ( $M_B^*$ ) but remain roughly constant in number density ( $\phi^*$ ). This visual assessment is confirmed by Schechter fits below. In short, for the whole population, galaxies are getting brighter with redshift, but their number density is remaining much the same, to  $z \sim 1$ .

*Blue galaxies (middle row):* The results found above for the All sample are repeated for the Blue sample, which is expected since blue galaxies dominate the total number of galaxies. This is shown in the middle row of Figure 7. The increasing separation between the points and black solid lines in each redshift bin relative to the DEEP2 fits at ( $0.2 \leq z < 0.4$ ) is easily seen, and the visual impression is that  $M_B^*$  brightens and  $\phi^*$  remains constant, again confirmed by Schechter fits below.

*Red galaxies (bottom row):* The bottom row of Figure 7 presents the data for red galaxies. As above, the dashed grey line represents the Schechter function fit to the lowest redshift bin of DEEP2 data. In contrast to blue galaxies, between  $z \sim 0.9$  and  $z \sim 0.3$ , the luminosity function of red galaxies in DEEP2 shows no evidence for large changes, with most variations in the number density, particularly at low  $z$ , being within the margins of cosmic variance. The only bin that shows some hint of change is the highest- $z$  bin, centered at  $z = 1.1$ , but which is likely to be the most affected by incompleteness (see below). Therefore the results from the DEEP2 survey alone are consistent with rather little change in the raw counts of red galaxies at bright magnitudes. If  $M_B^*$  and  $\phi^*$  are changing, they must do so in coordinated fashion such that the counts at fixed magnitude remain roughly constant. This behavior differs markedly from that of blue galaxies, where counts increase at fixed  $M_B$ .

These results are fairly robust relative to the adopted weighting model. The black points in Figure 7 use the average model of §3.3, which assumes that red galaxies without redshifts follow the same distribution as the observed ones. For an extreme test, the weighting was changed to a model where failed red galaxies (comprising about 25% of the total red galaxy sample) are *all placed in whatever redshift bin is being considered*. Here, red galaxies are defined as all objects with apparent  $R - I > 1.33$  (see line in Figure 1b). This extreme assumption clearly yields a *strict upper limit* to the red luminosity function in that bin. The test works well for red galaxies in the range  $z = 0.7 - 1.1$ , which all cluster strongly near observed  $R - I = 1.5$  (see Figure 1b).

This part of the apparent CM diagram thus contains all red galaxies that can possibly exist in this redshift range, unless large numbers are missing from the photometric catalog, which is unlikely, as discussed in §3.4. DEEP2 luminosity functions using this extreme incompleteness model are shown in Figure 8 as gray triangles. It is important to note that this model uses each failed red galaxy multiple times so the gray data points cannot be all valid simultaneously; they are strict upper lim-

its. The new correction does not increase the number of galaxies very much in the All function, since the total counts are dominated by blue galaxies, and the Red function is significantly impacted in only the most distant bin. Quantitative conclusions are drawn below by fitting Schechter functions.

#### 4.2. Schechter fits

The Schechter functions fits using the STY method are presented here. When splitting either galaxy sub-sample in narrow redshift bins, we see variations in the best-fitting faint-end slope that are not statistically significant, suggesting that we should average together slopes from several bins. In fact, the All galaxy function should show some trend because the ratio of red to blue galaxies changes with redshift and the shapes of the Red and Blue functions differ; however, the effect is small. As explained in more detail in Paper II, we decided to use the average faint-end slope values found within the range  $z = 0.2$  to  $0.6$  for the COMBO-17 sample, because of the much larger number of galaxies COMBO-17 contains in this redshift range in addition to there being no color pre-selection in that survey. The resulting values of the faint-end slope are  $\alpha = -0.5$  for the Red sample and  $\alpha = -1.3$  for the All and Blue samples; these were applied also to DEEP2 here. Even though several recent works have provided evidence of differential evolution between bright and faint red galaxies (e.g., McIntosh et al. 2005; Juneau et al. 2005; Treu et al. 2005), we adopt a fixed Schechter function in shape at all redshifts. The effect of varying the shape is small, as discussed in Paper II. The evolving Schechter parameters are presented in Table 3 for the All sample and in Tables 4 and 5 for the Blue and Red samples. Column (1) shows the central redshift of the bin; column (2) the number of galaxies used in the luminosity function calculation in each redshift bin; column (3) the value of the adopted faint-end slope,  $\alpha$ ; column (4) the value of  $M_B^*$ , followed by the upper and lower 68% Poisson errors in columns (5) and (6); the mean density  $\phi^*$  in column (7), followed by the 68% Poisson errors in columns (8) and (9); the square root of the cosmic variance error is shown in column (10); and (11) shows the luminosity density (in solar units) defined as

$$j_B(z) = \int L\phi(L)dL = L^* \phi^* \Gamma(\alpha + 2), \quad (20)$$

using  $M_{B\odot} = 5.48$  (Binney & Merrifield 1998), where  $\Gamma$  is the Gamma function, with the 68% Poisson error in column (12); column (13) indicates the weighting model (described in §3.3) used when calculating the fits. For the All and Red galaxy samples, the results using the the upper-limit method of §4.1 are also tabulated. The 68% Poisson errors for  $M_B^*$  and  $\phi^*$  were taken from the  $\Delta\chi^2 = 1$  contour levels in the  $(M_B^*, \phi^*)$  plane, computed from the  $1/V_{max}$  residuals and their errors relative to a given Schechter fit. Cosmic variance errors were computed as described above taking the volume and field geometry into account and using separate bias ( $b$ ) values for Blue and Red relative to the All galaxy sample. Errors for  $j_B$  were conservatively calculated by adding the fractional Poisson errors for  $M_B^*$  and  $\phi^*$  and cosmic variance in quadrature; these are an overestimate because this neglects the correlated errors in  $M_B^*$  and  $\phi^*$ , which

tend to conserve  $j_B$ . However, Poisson errors are generally smaller than cosmic variance, which is dominant, so this overestimate is small.

The changes of the Schechter parameters as a function of redshift are shown in Figure 11 for  $M_B^*$  (top row),  $\phi^*$  (middle row) and  $j_B$  (bottom row) for the All, Blue and Red galaxy samples. The figure shows results separately for minimal and average models, and in the case of the All sample, using the optimal model. As expected from the raw counts in Figure 7, the Schechter parameters for blue and red galaxies evolve differently with redshift. The brightening of blue galaxies is clearly seen, while their number density ( $\phi^*$ ) holds fairly steady. In contrast, red galaxies evolve only modestly in either  $M_B^*$  or  $\phi^*$ , and an increase in one quantity is balanced by the other keeping the total (red) luminosity density,  $j_B$ , roughly constant out to the very last bin, where it falls abruptly (see Table 5). The constancy of  $j_B$  for red galaxies was noted by Bell et al. (2004), who drew the conclusion that the total stellar mass of the red sequence must be falling as a function of increasing redshift. Paper II provides further evidence for this. For now, we simply note that the DEEP2 red counts agree well with the raw COMBO-17 red counts (as shown in Paper II), and with the conclusion by Bell et al. (2004) that  $j_B$  for red galaxies is constant.

The DEEP2 fitted values for  $\phi^*$  also show a formally significant drop back in time for red galaxies, a point which will be further discussed in Paper II.

The DEEP2 data were also used to explore if the different trends measured between red and blue galaxies can be detected when smaller subdivisions in the color-magnitude space are considered. For this, blue galaxies were subdivided using a line parallel to Equation (19) (which divides red from blue galaxies) but displaced downward in each redshift bin so it divides the blue galaxies into two equal halves. This line was calculated considering only galaxies brighter than  $M(z) = M_0 - Qz$ , where  $M_0 = -20$ , and  $Q$  is the amount of luminosity evolution (measured in magnitudes) per unit redshift, so that only the statistically similar populations of galaxies would be used. This method was used in preference to a constant color cut, which would yield a spurious evolution in numbers simply because blue galaxies are reddening with time (cf. Figure 4). Although this division does not use a clear feature as that dividing blue and red galaxies, it is calculated at roughly the average color of blue galaxies at a given absolute magnitude, and it allows testing whether the degree of evolution is somehow correlated with the average color of galaxies. When calculating Schechter function fits for Moderately Blue and Very Blue galaxies, we find that the fixed faint-end slope  $\alpha = -1.3$  used for the Blue galaxy sample provides a good description of both sub-samples, neither population shows significant evidence that the faint-end slope is changing with redshift. The evolution of  $M_B^*$ ,  $\phi^*$  and  $j_B$  for the subsamples of Moderately and Very Blue galaxies is shown in Figure 10. The top row shows how  $M_B^*$  changes with redshift, and it is readily apparent that the Moderately Blue galaxies are on average more luminous than the Very blue population. On the other hand, the number density of both populations (second row) does not show much evidence of significant changes; at all redshifts, the Very Blue galaxies present higher

number densities than the Moderately Blue population. The luminosity density (bottom row) shows that, except for the highest redshift bin ( $z \sim 1.3$ ), Moderately Blue galaxies output most of the optical light coming from the blue galaxy population. Overall both populations seem to evolve similarly, maintaining a constant offset in  $M_B^*$ , while  $\phi^*$  holds constant for both halves separately. These results show that from  $z \sim 1$  to the present, most of the light contributed by blue galaxies comes from galaxies with older stellar populations and/or greater dust reddening than the typical star-forming galaxy.

## 5. SUMMARY

A sample of more than 11,000 DEEP2 galaxies from  $z = 0.2-1.4$  is used to study the evolution of galaxy luminosity functions. When DEEP2 galaxies are plotted on the color-magnitude diagram ( $M_B$  vs.  $U - B$ ), blue and red galaxies occupy different loci, as seen in local samples, and this division is still clearly seen at  $z > 1.0$ . The bimodality in the color-magnitude plane of galaxies is used to subdivide the DEEP2 sample to study how luminosity functions evolve as a function of galaxy color. In order to account for the partial sampling strategy and redshift success rate of DEEP2 as a function of color and magnitude, weights are calculated using different models describing how failed redshifts are distributed in  $z$ . The current data suggest that the vast majority of faint and blue galaxies in the DEEP2 sample for which no redshifts were successfully measured are at high redshift ( $z > 1.4$ ). In this work we make the assumption that red galaxies with failed  $z$ 's follow roughly the same redshift distribution as the good measurements. Given the nature of redshift failures, a compromise approach where blue failures are assumed to be at high redshift (minimal), while red failures are assumed to follow the average model is regarded as optimal. The conclusions of this work hold independently of the adopted model.

The results from this work show that populations of blue and red galaxies evolve differently. As an ensemble, blue galaxies show a larger amount of luminosity evolution, yet show little change in overall number density. Red galaxies show less change in luminosity, but a larger change in number density. When the luminosity density is considered, blue galaxies show a steady decrease toward lower redshifts, while the luminosity density of red galaxies is almost constant.

Finally, we divided the blue galaxies using the a sloping line that splits the population into two equal halves at each redshift. We find that both halves are still adequately described by a fixed faint end slope of  $\alpha = -1.3$ , and that both sub-populations evolve in a similar manner. Even in our highest redshift bins, the adopted shape of the faint end still provides a good description of the data, with no strong evidence of an increase in numbers of Very Blue galaxies at the lowest luminosity limit we probe.

A detailed comparison between the results obtained for the DEEP2 survey (this paper) with other works (Wolff et al. 2003; Bell et al. 2004; Gabasch et al. 2004; Ilbert et al. 2005) shows a good agreement. The combined results of these surveys are presented in Paper II (Faber et al. 2005), suggesting that the luminosity function of galaxies to  $z \sim 1$ , is currently well understood. The present paper presents the results using about a quar-



ter of the planned DEEP2 data, and shows the potential that DEEP2 has in characterizing the properties of galaxy populations to  $z \sim 1.2$ . As the DEEP2 survey reaches completion, ancillary data coming from  $Z$ -band photometry by Lin and collaborators are also being obtained in DEEP2 Fields 2-4. These will allow measuring photometric redshifts for galaxies in these three fields, and will allow a far more precise characterization of the properties of galaxies with “failed” redshifts. This, combined with a  $4 \times$  larger sample with spectroscopic redshifts, will constitute for many years to come the main sample of galaxies at redshifts  $0.7 \leq z \leq 1.4$ , that can be used to study how galaxy populations change with time. The data for Fields 2-4 used in this paper can be retrieved from <http://deep.berkeley.edu/DR1>. The second data release, tentatively scheduled for late 2005, will include all the data which were used in the analysis of this paper.

The DEEP team thanks C. Wolf for several discussions regarding the color-separated luminosity function and C. Steidel for sharing unpublished redshift data. CNAW thanks G. Galaz, S. Rauzy, M. A. Hendry and K. D’Mellow for extensive discussions on the measurement of the luminosity function. Suggestions from the anonymous referee are gratefully acknowledged. The authors thank the Keck Observatory staff for their constant support during the several observing runs of DEEP2; the W.

M. Keck Foundation and NASA for construction of the Keck telescopes. The DEIMOS spectrograph was funded by NSF grant ARI92-14621 and by generous grants from the California Association for Research in Astronomy, and from UCO/Lick Observatory. We also wish to recognize and acknowledge the highly significant cultural role and reverence that the summit of Mauna Kea has always had within the indigenous Hawaiian community. It is a privilege to be given the opportunity to conduct observations from this mountain. Support from National Science Foundation grants 00-71198 to UCSC and AST 00-71048 to UCB is gratefully acknowledged. SMF would like to thank the California Association for Research in Astronomy for a generous research grant and the Miller Institute at UC Berkeley for the support of a visiting Miller Professorship. JAN acknowledges support by NASA through Hubble Fellowship grant HST-HF-01132.01 awarded by the Space Telescope Science Institute, which is operated by AURA Inc. under NASA contract NAS 5-26555. Computer hardware gifts from Sun Microsystems and Quantum, Inc. are gratefully acknowledged. This research has made use of the NASA/IPAC Extragalactic Database (NED), which is operated by the Jet Propulsion Laboratory, California Institute of Technology, under contract with the National Aeronautics and Space Administration. Finally, we acknowledge NASA’s (indispensable) Astrophysics Data System Bibliographic Services.

#### REFERENCES

- Azusienis, A. & Straizys, V. 1969, *Soviet Astron.*, 13, 316  
 Baldry, I. K., Glazebrook, K., Brinkmann, J., Ivezić, Z., Lupton, R. H., Nichol, R. C., & Szalay, A. S. 2004, *ApJ*, 600, 681  
 Bell, E. F., et al. 2004, *ApJ*, 608, 752  
 Binggeli, B., Sandage, A., & Tammann, G. A. 1988, *ARA&A*, 26, 509  
 Binney, J. & Merrifield, M. 1998, *Galactic Astronomy* (Princeton: Princeton University Press)  
 Blanton, M. R., et al. 2001, *AJ*, 121, 2358  
 Blanton, M. R., et al., 2003, *ApJ*, 592, 819  
 Bruzual, G., & Charlot, S. 2003, *MNRAS*, 344, 1000  
 Buser, R. 1978, *A&A*, 70, 555  
 Choloniewski, J. 1986, *MNRAS*, 223, 1  
 Coil, A. L., et al. 2004a, *ApJ*, 609, 525  
 Coil, A. L., et al. 2004b, *ApJ*, 617, 765  
 Colless, M. et al. 2001, *MNRAS*, 328, 1039  
 Cuillandre, J.-C., Luppino, G., Starr, B., & Isani, S. 2001, in *Proceedings of Semaine de l’Astrophysique Française*, eds. F. Combes, D. Barret, F. Thévenin (Les Ulis: EdP-Sciences), 605  
 Davis, M., & Huchra, J. P. 1982, *ApJ*, 254, 437  
 Davis, M., et al. 2003, *SPIE*, 4834, 161  
 de Lapparent, V., Arnouts, S., Galaz, G., & Bardelli, S. 2003, *A&A*, 404, 845  
 de Vaucouleurs, G., de Vaucouleurs, A., Corwin, H. G., Buta, R. J., Paturel, G., & Fouqué, P. 1991, *The Third Reference Catalog of Galaxies* (New York: Springer Verlag) (RC3)  
 Eales, S. 1993, *ApJ*, 404, 51  
 Efsthathiou, G., Ellis, R. S., & Peterson, B. A. 1988, *MNRAS*, 232, 441  
 Ellis, R. S., Colless, M., Broadhurst, T., Heyl, J. & Glazebrook, K. 1996, *MNRAS*, 280, 235  
 Faber, S. M., et al. 2003, *SPIE*, 4841, 1657  
 Faber, S. M., et al. 2005, in preparation (Paper II)  
 Felten, J. E. 1976, *ApJ*, 207, 700  
 Fukugita, M., Shimasaku, K. & Ichikawa, T. 1995, *PASP* 107, 945  
 Gabasch, A., et al. 2004, *A&A*, 421, 41  
 Gebhardt, K. et al. 2003, *ApJ*, 597, 239  
 Giallongo, E. et al. 2005, *ApJ*, 622, 116  
 Hogg, D. W., Baldry, I. K., Blanton, M. R., & Eisenstein, D. J. 2002, *astro-ph/0210394*  
 Hogg, D. et al. 2003, *ApJ*, 585, 5  
 Ilbert, O., et al. 2005, *A&A*, 439, 863  
 Im, M., et al. 2002, *ApJ*, 571, 1361  
 Juneau, S., et al. 2005, *ApJ*, 619, L135  
 Kaiser, N., Squires, G., & Broadhurst, T. 1995, *ApJ*, 449, 460  
 Kauffmann, G., et al. 2003, *MNRAS*, 341, 33  
 Kinney, A. L., Calzetti, D., Bohlin, R. C., McQuade, K., Storchi-Bergmann, T., & Schmitt, H. R. 1996, *ApJ*, 467, 38  
 Kodama, T., Balogh, M. L., Smail, I., Bower, R. G., & Nakata, F. 2004, *MNRAS*, 354, 1103  
 Lilly, S. J., Tresse, L., Hammer, F., Crampton, D., & Le Fèvre, O. 1995, *ApJ*, 455, 108  
 Lin, H., Yee, H. K. C., Carlberg, R. G., Morris, S. L., Sawicki, M., Patton, D. R., Wirth, G., & Shepherd, C. W. 1999, *ApJ*, 518, 533  
 Lynden-Bell, D. 1971, *MNRAS*, 155, 95  
 Madgwick, D., et al. 2002, *MNRAS*, 333, 133  
 Madgwick, D., et al. 2003, *ApJ*, 599, 997

- Marzke, R. O., Huchra, J. P., & Geller, M. J. 1994, ApJ, 428, 43
- McIntosh, D., et al., 2005, ApJ, 632, 191
- Newman, J. A., & Davis, M. 2002, ApJ, 564, 567
- Norberg, P., Cole, S., Baugh, C. M., et al. 2002, MNRAS, 336, 907
- Oke, J. B., & Sandage, A. 1962, ApJ, 154, 21
- Page, M. J., & Carrera, F. J. 2000, MNRAS, 311, 433
- Press, W. H., Flannery, B. P., Teukolsky, S. A., Vetterling, W. T. 1986, *Numerical Recipes*, (Cambridge: Cambridge Univ. Press) 536, 79
- Sandage, A., Tammann, G. A., & Yahil, A. 1979, ApJ, 172, 253 (STY)
- Schechter, P. L. 1976, ApJ, 203, 297
- Schlegel, D. J., Finkbeiner, D. P., & Davis, M. 1998, ApJ, 500, 525
- Schmidt, M. 1968, ApJ, 151, 393
- Simard, L., et al. 2002, ApJS, 142, 1
- Strateva, I., et al. 2001, AJ, 122, 1861
- Takeuchi, T. T., Yoshikawa, K., & Ishii, T. T. 2000, ApJS, 120, 1
- Tresse, L. 1999, in “Formation and Evolution of Galaxies”, eds. O. Le Fèvre and S. Charlot, Les Houches School Series, Springer-Verlag, astro-ph/9902209
- Treu, T., Ellis, R. S., Liao, T. L., & van Dokkum, P. G. 2005, ApJ, 622, L5
- Turner, E. L. 1979, ApJ, 231, 645
- van Dokkum, P. G., Franx, M., Fabricant, D., Illingworth, G. D., & Kelson, D. D. 2000, ApJ, 541, 95
- Weiner, B. J., Phillips, A. C., et al. 2005, ApJ, accepted
- Willmer, C. N. A. 1997, AJ, 114, 898
- Wolf, C., Meisenheimer, K., Rix, H.-W., Borch, A., Dye, S., & Kleinheinrich, M. 2003, A&A, 401, 73
- York, D. et al. 2000, AJ, 120, 1579
- Zucca, E., Pozzetti, L., & Zamorani, G. 1994, MNRAS, 269, 953

Figure 1 is available as 0506041.f1.jpg

FIG. 1.— Apparent color-magnitude distribution of galaxies in the DEEP2 Survey. Panel *a* shows the full sample, panel *b* the distribution of galaxies set on slits, and panel *c* the distribution of successful redshifts, where galaxies in the main DEEP2 redshift interval are shown as green crosses, galaxies lying beyond the upper redshift limit adopted in this work ( $z = 1.4$ ) are shown as red diamonds, and galaxies below the main redshift limit adopted here ( $z = 0.8$ ) are black plusses. Panel *d* shows the distribution of failed redshifts. The  $R_{AB}$  limiting magnitude of 24.1, transformed into  $R_{Vega} = 23.88$ , is shown as the vertical dotted line. The ridge of galaxies at blue colors ( $\bar{R} - I \sim 0.5$ ) is dominated by galaxies at redshifts below the DEEP2 pre-selection color cut at  $z = 0.7$ ; faint ones also include many distant galaxies with  $z > 1.4$ . The bimodal distribution seen in rest-frame colors (cf. Figure 4) is also seen in observed  $R - I$ ; the horizontal dashed line in panel *b* shows the dividing line for the extreme red-galaxy correction function used in §4.1 at  $R - I = 1.33$ . Dashed grey lines show the boundaries used in the redshift histograms displayed in Figure 2.

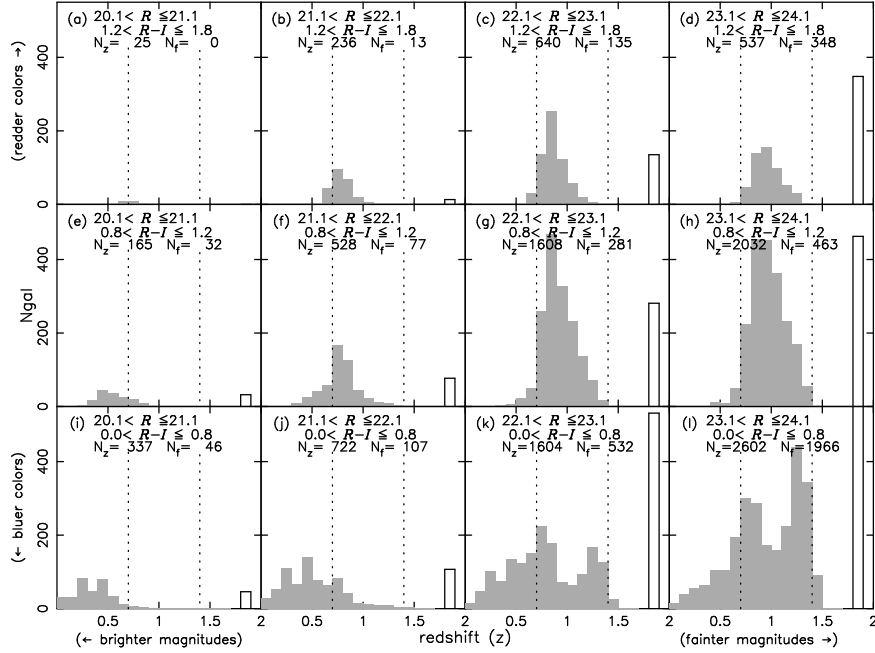


FIG. 2.— Raw redshift distributions of DEEP2 galaxies in the apparent color-magnitude bins indicated in Figure 1. Magnitudes become fainter towards the right and colors redder towards the top. The color boundaries were chosen to correspond roughly to the main loci of galaxies in rest-frame color-magnitude space: the top four panels correspond to galaxies on the red sequence, while the middle panels correspond to intermediate colors, i.e.,  $(U - B) \leq -0.3$  mag bluer than the red sequence, as outlined by the middle dotted line in Figure 4. The lower panels represent galaxies bluer than this. The vertical dashed lines represent the low- and high- $z$  design limits for Fields 2, 3, and 4 of DEEP2 ( $z = 0.7$  and  $1.4$  respectively); galaxies at lower redshifts come mainly from Field 1 (EGS). No attempt is made in this plot to correct for the different slit assignment algorithm used for EGS and Fields 2-4. Failed redshifts are represented by the bars to the right of each panel; the one at lower right has been truncated to 550 galaxies. The total number of galaxies plotted is shown in each panel, where  $N_z$  represents the number of good measurements and  $N_f$  the number of failures. The bimodal distribution in redshift seen in the two fainter magnitude bins for blue galaxies is an artifact caused by the shift of the  $4000 \text{ \AA}$  break into and out of the  $R$  and  $I$  filters as a function of redshift. When both filters are redder than  $4000 \text{ \AA}$  the colors are flat, then become red, then flatten again once both filters are bluer than rest-frame  $4000 \text{ \AA}$ .

Figure 3 is available as 0506041.f3.jpg

FIG. 3.— Rest-frame  $U - B$  as a function of redshift for DEEP2 galaxies. The  $U - B$  values in this paper are corrected for Galactic extinction but not for internal galactic extinction. The bimodal distribution of colors is clearly seen to  $z \sim 1$ . Fields 2, 3, and 4 lack low-redshift objects because of the pre-selection color cut; this cut was not applied to Field 1 (EGS), but a secondary redshift selection still applies to this field, as explained in the text. The lack of low-redshift red galaxies (in EGS) is likely due to the combination of the relative paucity of red galaxies, the small volume at low redshifts, and the bright apparent magnitude cut of the sample. All fields show clustering, and the observed variations are due to cosmic variance.

Figure 4 is available as 0506041.f4.jpg

FIG. 4.— Rest-frame color-magnitude diagrams for DEEP2 for the redshift intervals used in this work. The three lower  $z$  intervals (panels  $a$ ,  $b$  and  $c$ ) contain only EGS data, while galaxies in all four DEEP2 fields are shown for  $z \geq 0.8$ . The solid line in each panel indicates the approximate faint absolute magnitude limit as a function of intrinsic color and redshift for a sample with a fixed apparent magnitude limit  $R_{Vega} = 23.88$ . This line is calculated at the *upper* redshift limit of each panel and denotes the limiting magnitude for which a volume-limited sample could be defined in that bin. This calculation uses the distance modulus and the K-correction appropriate for each template SED, which is then fit by a linear relation, corresponding to the plotted line. The dashed lines repeat the same lines in other panels. The upper dotted line denotes the cut used to define red-sequence galaxies (Equation 19) and is the same at all redshifts. The lower dotted line is drawn parallel to this, but its vertical height is displaced downward in each redshift bin to divide Very Blue from Moderately Blue galaxies into two equal halves (see §4.2). The numbers in each panel show the number of galaxies plotted and the co-moving volume in  $\text{Mpc}^3$  for the  $(H_0, \Omega, \Lambda) = (70, 0.3, 0.7)$  cosmology.

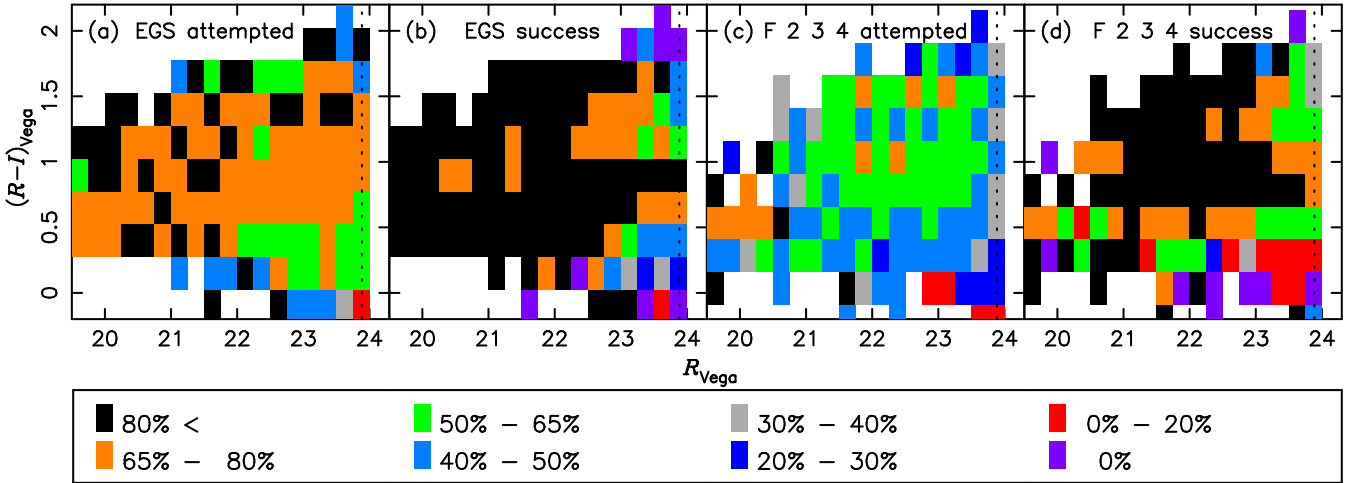


FIG. 5.— Sampling and redshift success rates as a function of apparent magnitude and  $R - I$  color for DEEP2. The colors, coded in the key, correspond to the sampling rate (panels  $a$  and  $c$ ) or redshift success rate (panels  $b$  and  $d$ ). In all panels, the black dotted line corresponds to the limiting apparent magnitude  $R_{Vega} = 23.88$ . Panels  $a$  and  $b$  refer to the Extended Groth Strip, while panels  $c$  and  $d$  show Fields 2, 3, and 4. Panels  $a$  and  $c$  show the percentage of galaxies placed on slits relative to the total sample (for EGS, the total sample is all galaxies in each  $R, R - I$  bin; for Fields 2, 3, and 4, it is the target galaxies photometrically selected to have  $> 0.7$ ). Panels  $b$  and  $d$  show the success rate for good redshifts of those attempted. The difference in sampling rates between the EGS and Fields 2-4 is caused by differences in the density of targets and slitmasks on the sky for these fields, along with changes to the weights given faint objects made after the early data from Fields 2-4 were obtained.

Figure 6 is available as 0506041.f6.jpg

FIG. 6.— Weights used to correct for incomplete sampling and failed redshifts. Panels *a* and *b* show galaxies in EGS with  $z < 0.8$ , while panels *c* and *d* show galaxies in all four fields with  $z \geq 0.8$ . Weights are shown here as a function of  $R$  vs.  $R - I$ . In actuality, they are calculated in bins of color-color-magnitude space, incorporating  $B - R$  as well. Panels *a* and *c* show the weight of each galaxy using the “minimal” model, in which all galaxies with failed redshifts are assumed to lie above the upper redshift limit of the survey ( $z = 1.4$ ). Panels *b* and *d* show how the galaxy weights change in moving from the minimal model to the “average” model, in which failed galaxies are assumed to be distributed in  $z$  like the observed ones.

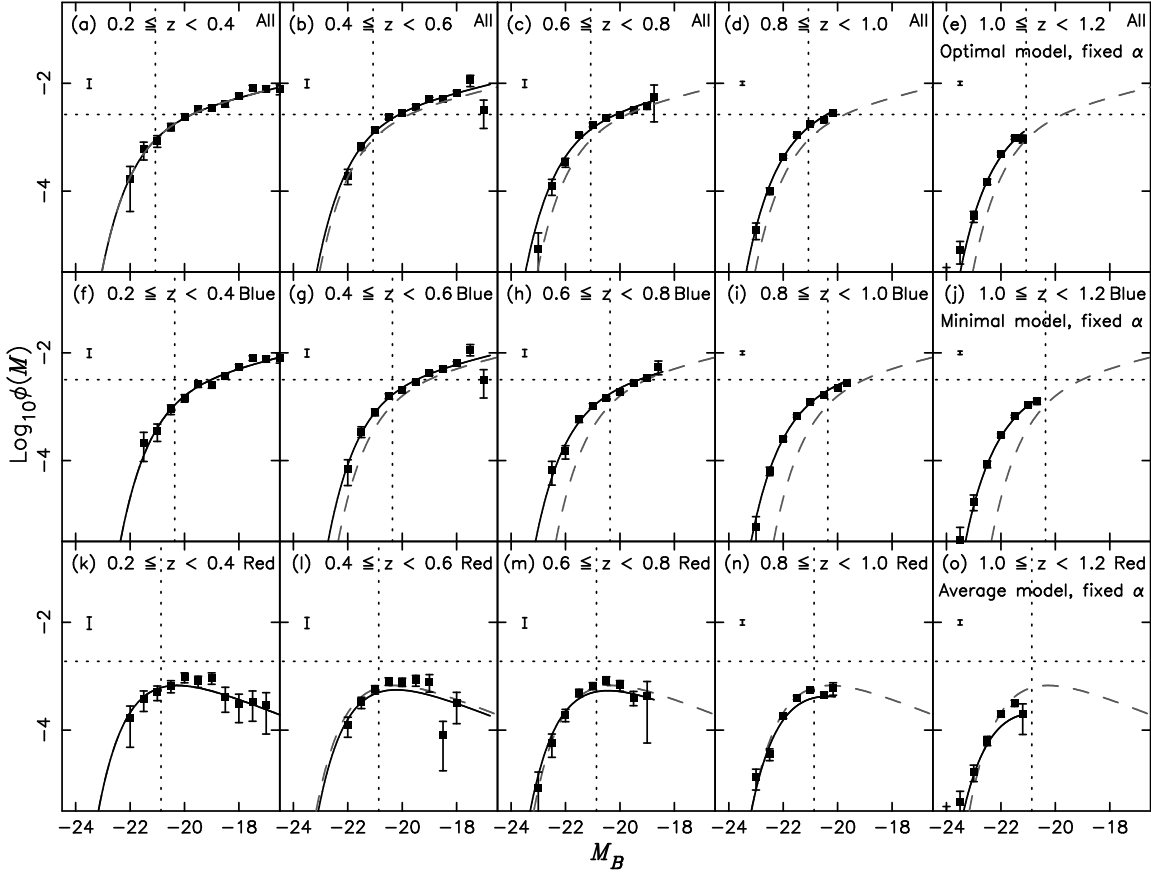


FIG. 7.— Luminosity functions measured in different redshift bins for “All” galaxies (top row), “Blue” galaxies (middle row), and “Red” galaxies (bottom row). Points calculated using the  $1/V_{max}$  method are shown as black squares. Error bars represent the 68% Poisson error bars only. Errors due to cosmic variance (calculated as described in the text) are shown at the top left of each panel. The values plotted use the favored models to correct for the incomplete sampling rate and redshift failures (see text). The solid black lines represent the STY fits to DEEP2 data, keeping the faint-end slope  $\alpha$ 's fixed at the values measured from the COMBO-17 “quasi-local” sample in three redshift bins of  $\Delta z = 0.2$  width, ranging from  $z = 0.2 - 0.6$  (see Paper II). The values assumed are  $\alpha = -1.3$  (All),  $\alpha = -1.3$  (Blue), and  $\alpha = -0.5$  (Red). The dashed grey curves show the Schechter function fits to the lowest redshift bin measured by DEEP2 and are repeated in each panel for All, Blue and Red galaxies respectively. The dotted lines serve as a visual reference and are plotted at the values of  $M_B^*$  and  $\phi^*$  for the lowest redshift interval. The main conclusion from this figure is that blue and red luminosity functions evolve differently: blue counts at fixed absolute magnitude increase markedly back in time, while red counts tend to remain constant.

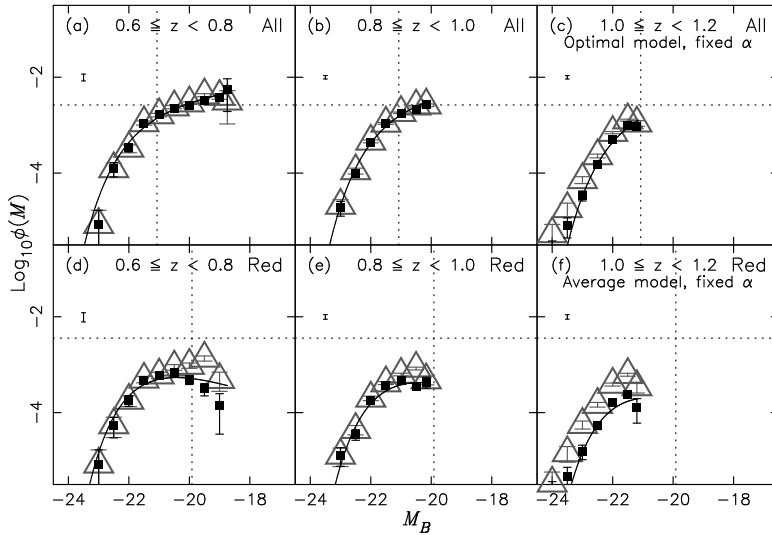


FIG. 8.— Luminosity function for DEEP2 All and Red galaxy samples. The change relative to Figure 7 is the addition of the grey triangles, which are strict upper limits to the density of galaxies under the extreme assumption that all failed-redshift red galaxies are located in that bin only. This model uses each failed red galaxy more than once, and thus all grey triangles cannot be valid simultaneously. Only in the highest redshift bin does the use of this assumption cause a significant increase in the number density of red galaxies. The solid black lines show the same parametric fits as in Figure 7.

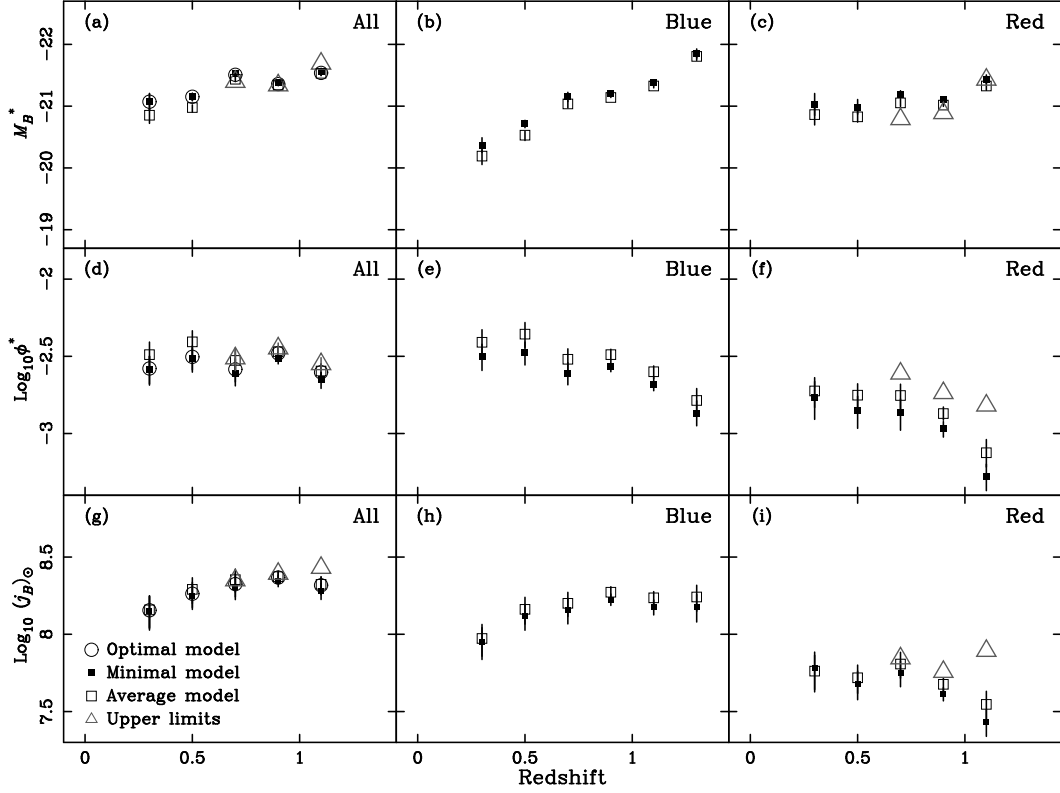


FIG. 9.— Evolution of the Schechter function parameters  $M_B^*$ ,  $\phi^*$  and  $j_B$  assuming constant  $\alpha$ , as a function of redshift. The solid black squares show the values measured using the minimal weight model, open squares show the values for the average model, and open circles the optimal model. Because blue galaxies dominate the total numbers of galaxies, the results using optimal and minimal weights are very similar. The minimal model is preferred for Blue, while the average model is preferred for Red galaxies (see text). The open triangles represent the fit values making the extreme assumption that all red galaxies for which no redshift could be measured are located in the  $z = 0.7, 0.9$  and  $1.1$  bins respectively, providing absolute upper limits for the Schechter parameters. The difference in the mode of evolution for blue and red galaxies is clearly seen. The quantity  $M_B^*$  increases markedly back in time for blue galaxies, while number density  $\phi^*$  holds roughly constant (to  $z = 1$ ). The net effect is that  $j_B$  for blue galaxies is increasing with redshift. Magnitude evolution of red galaxies is milder, though  $\phi^*$  may drop more. The net effect is that  $j_B$  for red galaxies remains relatively constant than for blue galaxies to  $z = 0.9$ , but may drop beyond that.

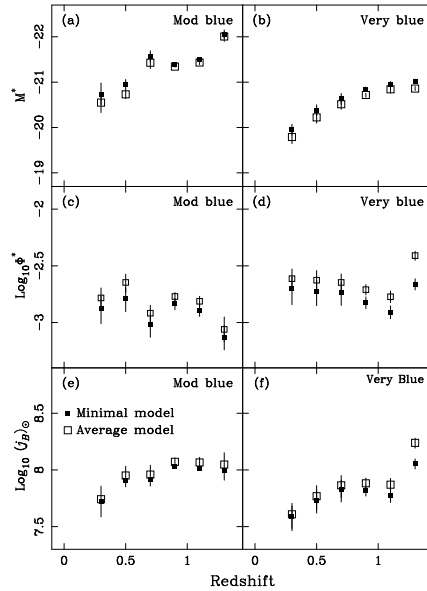


FIG. 10.— Evolution of the Schechter function parameters  $M_B^*$ ,  $\phi^*$  and  $j_B$  assuming constant  $\alpha$ , as a function of redshift for Moderately Blue and Very Blue galaxies. The solid black squares show the values measured using the minimal weight model, while open squares show the values for the average model. On average, the Moderately Blue galaxies are brighter than the Very Blue galaxies, both populations showing a comparable brightening back in time. The number density of Very Blue galaxies is always slightly higher than of Moderately Blue galaxies, and both populations show small changes back in time. Both Moderately Blue and Very Blue galaxies show a steady increase in luminosity density as higher redshifts are reached. Up to  $z \sim 1.1$ , the  $j_B$  measurements suggest that the bulk of the light from blue galaxies comes from the Moderately Blue population. Overall the properties of both populations of galaxies show a similar evolutionary trend. These results from  $j_B$  suggest that to redshifts reached by DEEP2, the optical light from galaxies is not dominated by newly-formed stars but rather by a combination of these with older stellar populations.



TABLE 1  
CONVERSION BETWEEN AB AND VEGA MAGNITUDES

Transformation		System
$U_{AB}$	$= U_{Vega} + 0.73$	Johnson
$B_{AB}$	$= B_{Vega} - 0.10$	Johnson
$(U - B)_{AB}$	$= (U - B)_{Vega} + 0.81$	Johnson
$B_{AB}$	$= B_{Vega} - 0.11$	CFHT 12K×8K B
$R_{AB}$	$= R_{Vega} + 0.22$	CFHT 12K×8K R
$I_{AB}$	$= I_{Vega} + 0.44$	CFHT 12K×8K I
$(B - R)_{AB}$	$= (B - R)_{Vega} - 0.33$	CFHT 12K×8K
$(R - I)_{AB}$	$= (R - I)_{Vega} - 0.22$	CFHT 12K×8K

Note. – The procedure used to calculate these transformations is described in Appendix A

TABLE 2  
SURVEY CHARACTERISTICS

Survey	Area $\square^\circ$	$N_{field}$	$N_{gal}$	$N_z$	$N_z > 0.8$	$m_l$	$m_u$	$z_{min}$	$z_{max}$	System
(1)	(2)	(3)	(4)	(5)	(6)	(7)	(8)	(9)	(10)	(11)
EGS	0.28	1	9115	4946	2026	18.5	24.1	0.2	1.4	$R_{AB}$
Fields 2+3+4	0.85	3	18756	6338	4820	18.5	24.1	0.8	1.4	$R_{AB}$

Note. – The meanings of columns are: (1) Surveyed region; (2) area in square degrees; (3) number of non-contiguous fields in surveyed region; (4) number of galaxies in source catalogue; (5) number of good quality redshifts; (6) number of good quality redshifts above  $z = 0.8$ ; (7) bright apparent magnitude limit; (8) faint apparent magnitude limit; (9) lower redshift limit; (10) upper redshift limit; (11) apparent magnitude system of catalogue.

TABLE 3  
SCHECHTER FUNCTION PARAMETERS FOR ALL GALAXY SAMPLES

$\langle z \rangle$	$N_{gal}$	$\alpha$	$M_B^*$		$\phi^*$		$\sqrt{Var}$	$j_B$	Weights			
(1)	(2)	(3)	(4)	(5)	(6)	(7)	(8)	(9)	(10)	(11)	(12)	(13)
						$\times 10^{-4}$	Gal Mpc $^{-3}$			$\times 10^8$	$L_\odot$	
0.30	734	-1.30	-21.07	(+ 0.13 - 0.14)	26.08	(+ 2.10 - 2.12)	0.20	1.41 $\pm$ 0.35	minimal			
0.50	983	-1.30	-21.16	(+ 0.05 - 0.07)	30.40	(+ 0.97 - 0.98)	0.18	1.78 $\pm$ 0.33	minimal			
0.70	914	-1.30	-21.53	(+ 0.03 - 0.03)	24.43	(+ 0.75 - 0.80)	0.16	2.02 $\pm$ 0.34	minimal			
0.90	2561	-1.30	-21.38	(+ 0.01 - 0.02)	30.81	(+ 0.30 - 0.63)	0.08	2.22 $\pm$ 0.19	minimal			
1.10	844	-1.30	-21.57	(+ 0.05 - 0.04)	22.36	(+ 2.09 - 1.39)	0.08	1.91 $\pm$ 0.23	minimal			
0.30	740	-1.30	-20.85	(+ 0.10 - 0.13)	32.46	(+ 1.88 - 2.14)	0.20	1.44 $\pm$ 0.34	average			
0.50	983	-1.30	-20.98	(+ 0.04 - 0.08)	39.26	(+ 1.94 - 1.65)	0.18	1.95 $\pm$ 0.37	average			
0.70	919	-1.30	-21.44	(+ 0.04 - 0.04)	29.77	(+ 0.99 - 0.90)	0.16	2.26 $\pm$ 0.39	average			
0.90	2436	-1.30	-21.34	(+ 0.03 - 0.01)	33.98	(+ 0.60 - 0.39)	0.08	2.37 $\pm$ 0.20	average			
1.10	805	-1.30	-21.53	(+ 0.04 - 0.03)	25.43	(+ 2.20 - 1.88)	0.08	2.11 $\pm$ 0.25	average			
0.30	734	-1.30	-21.07	(+ 0.13 - 0.13)	26.39	(+ 1.81 - 1.62)	0.20	1.43 $\pm$ 0.33	optimal			
0.50	983	-1.30	-21.15	(+ 0.06 - 0.06)	31.39	(+ 0.97 - 1.04)	0.18	1.83 $\pm$ 0.32	optimal			
0.70	914	-1.30	-21.51	(+ 0.03 - 0.03)	26.07	(+ 1.39 - 1.14)	0.16	2.11 $\pm$ 0.34	optimal			
0.90	2561	-1.30	-21.36	(+ 0.01 - 0.02)	33.04	(+ 0.90 - 1.11)	0.08	2.33 $\pm$ 0.20	optimal			
1.10	844	-1.30	-21.54	(+ 0.04 - 0.04)	24.94	(+ 2.20 - 2.63)	0.08	2.08 $\pm$ 0.27	optimal			
0.70	1059	-1.30	-21.39	(+ 0.04 - 0.05)	30.70	(+ 0.86 - 1.08)	0.16	2.24 $\pm$ 0.42	upper limit			
0.90	2844	-1.30	-21.34	(+ 0.01 - 0.01)	35.60	(+ 0.83 - 0.22)	0.08	2.47 $\pm$ 0.40	upper limit			
1.10	1210	-1.30	-21.69	(+ 0.05 - 0.04)	28.15	(+ 1.70 - 1.73)	0.08	2.69 $\pm$ 0.46	upper limit			

Note. – The meanings of columns are: (1) central redshift of bin; (2) number of galaxies in bin; (3) the value of the adopted faint-end slope; (4) the value of  $M_B^*$ , and upper (5) and lower (6) 68% Poisson errors; (7) mean density  $\phi^*$  followed by the 68% Poisson errors in columns (8) and (9); (10) square root of the fractional cosmic variance error, based on field geometry, bin volume and galaxy bias ( $b$ ) as a function of color (see text) (11) luminosity density, followed in (12) by a conservative error that combines Poisson errors in  $M_B^*$  and  $\phi^*$  with cosmic variance in quadrature; see text for further explanation. (13) indicates whether the fits were calculated using the minimal, average or optimal weighting schemes, as described in §3.3, or placing all failed red galaxies at  $z = (0.7, 0.9, 1.1)$ , as described in §4.1

TABLE 4  
SCHECHTER FUNCTION PARAMETERS FOR BLUE GALAXY SAMPLES

$\langle z \rangle$	$N_{gal}$	$\alpha$	$M_B^*$		$\phi^*$		$\sqrt{Var}$	$j_B$	Weights			
(1)	(2)	(3)	(4)	(5)	(6)	(7)	(8)	(9)	(10)	(11)	(12)	(13)
						$\times 10^{-4}$	Gal Mpc $^{-3}$			$\times 10^8$	$L_\odot$	
0.30	627	-1.30	-20.36	(+ 0.13 - 0.11)	31.78	(+ 2.15 - 1.87)	0.18	0.89 $\pm$ 0.20	minimal			
0.50	812	-1.30	-20.72	(+ 0.05 - 0.07)	33.40	(+ 1.39 - 1.77)	0.16	1.31 $\pm$ 0.23	minimal			
0.70	764	-1.30	-21.15	(+ 0.07 - 0.07)	24.67	(+ 1.35 - 1.58)	0.15	1.44 $\pm$ 0.26	minimal			
0.90	2644	-1.30	-21.21	(+ 0.00 - 0.03)	27.27	(+ 0.35 - 0.42)	0.08	1.68 $\pm$ 0.13	minimal			
1.10	1224	-1.30	-21.38	(+ 0.04 - 0.05)	20.84	(+ 1.08 - 1.58)	0.08	1.50 $\pm$ 0.16	minimal			
1.30	448	-1.30	-21.86	(+ 0.07 - 0.08)	13.44	(+ 2.00 - 2.71)	0.07	1.51 $\pm$ 0.31	minimal			
0.30	627	-1.30	-20.19	(+ 0.10 - 0.14)	38.98	(+ 1.99 - 2.73)	0.18	0.94 $\pm$ 0.21	average			
0.50	812	-1.30	-20.53	(+ 0.06 - 0.09)	44.07	(+ 2.05 - 2.97)	0.16	1.45 $\pm$ 0.27	average			
0.70	764	-1.30	-21.04	(+ 0.05 - 0.06)	30.25	(+ 1.36 - 1.25)	0.15	1.59 $\pm$ 0.27	average			
0.90	2644	-1.30	-21.14	(+ 0.03 - 0.00)	32.43	(+ 0.55 - 0.35)	0.08	1.87 $\pm$ 0.15	average			
1.10	1224	-1.30	-21.33	(+ 0.03 - 0.03)	25.13	(+ 1.29 - 1.01)	0.08	1.72 $\pm$ 0.16	average			
1.30	448	-1.30	-21.81	(+ 0.06 - 0.06)	16.39	(+ 2.55 - 2.94)	0.07	1.75 $\pm$ 0.33	average			

Note. – The meanings of columns are the same as in Table 3.

TABLE 5  
SCHECHTER FUNCTION PARAMETERS FOR RED GALAXY SAMPLES

$\langle z \rangle$	$N_{gal}$	$\alpha$	$M_B^*$		$\phi^*$		$\sqrt{Var}$	$j_B$	Weights			
(1)	(2)	(3)	(4)	(5)	(6)	(7)	(8)	(9)	(10)	(11)	(12)	(13)
						$\times 10^{-4}$	Gal Mpc $^{-3}$			$\times 10^8$	$L_\odot$	
0.30	109	-0.50	-21.02	(+ 0.18 - 0.17)	17.06	(+ 1.65 - 1.64)		0.26	0.60 $\pm$ 0.16	minimal		
0.50	173	-0.50	-20.97	(+ 0.14 - 0.10)	14.15	(+ 0.70 - 0.62)		0.23	0.48 $\pm$ 0.10	minimal		
0.70	196	-0.50	-21.19	(+ 0.06 - 0.06)	13.66	(+ 1.09 - 1.00)		0.22	0.56 $\pm$ 0.10	minimal		
0.90	535	-0.50	-21.11	(+ 0.04 - 0.05)	10.72	(+ 0.38 - 0.36)		0.11	0.41 $\pm$ 0.04	minimal		
1.10	178	-0.50	-21.44	(+ 0.07 - 0.08)	5.24	(+ 0.79 - 0.95)		0.11	0.27 $\pm$ 0.05	minimal		
0.30	109	-0.50	-20.86	(+ 0.16 - 0.17)	18.89	(+ 1.89 - 1.85)		0.26	0.58 $\pm$ 0.18	average		
0.50	173	-0.50	-20.83	(+ 0.12 - 0.09)	17.71	(+ 1.03 - 1.13)		0.23	0.52 $\pm$ 0.13	average		
0.70	196	-0.50	-21.05	(+ 0.06 - 0.06)	17.63	(+ 1.29 - 1.50)		0.22	0.64 $\pm$ 0.15	average		
0.90	535	-0.50	-21.02	(+ 0.04 - 0.02)	13.47	(+ 0.60 - 0.82)		0.11	0.47 $\pm$ 0.06	average		
1.10	178	-0.50	-21.33	(+ 0.08 - 0.07)	7.51	(+ 1.31 - 1.52)		0.11	0.35 $\pm$ 0.08	average		
0.70	334	-0.50	-20.79	(+ 0.08 - 0.07)	24.46	(+ 1.41 - 1.71)		0.22	0.70 $\pm$ 0.14	upper limit		
0.90	848	-0.50	-20.89	(+ 0.03 - 0.03)	18.28	(+ 0.83 - 0.38)		0.11	0.57 $\pm$ 0.10	upper limit		
1.10	548	-0.50	-21.43	(+ 0.05 - 0.04)	15.19	(+ 0.85 - 1.21)		0.11	0.78 $\pm$ 0.13	upper limit		

Note. – The meanings of columns are the same as in Table 3.

TABLE 6  
SCHECHTER FUNCTION PARAMETERS FOR MODERATELY BLUE GALAXY SAMPLE

$\langle z \rangle$	$N_{gal}$	$\alpha$	$M_B^*$		$\phi^*$		$\sqrt{Var}$	$j_B$	Weights			
(1)	(2)	(3)	(4)	(5)	(6)	(7)	(8)	(9)	(10)	(11)	(12)	(13)
						$\times 10^{-4}$	Gal Mpc $^{-3}$			$\times 10^8$	$L_\odot$	
0.30	306	-1.30	-20.73	(+ 0.25 - 0.22)	13.42	(+ 1.18 - 1.32)		0.18	0.53 $\pm$ 0.16	minimal		
0.50	440	-1.30	-20.96	(+ 0.10 - 0.11)	16.43	(+ 1.09 - 0.78)		0.16	0.80 $\pm$ 0.16	minimal		
0.70	372	-1.30	-21.57	(+ 0.13 - 0.11)	9.58	(+ 0.59 - 0.66)		0.15	0.82 $\pm$ 0.16	minimal		
0.90	1605	-1.30	-21.40	(+ 0.03 - 0.03)	14.59	(+ 0.29 - 0.55)		0.08	1.07 $\pm$ 0.09	minimal		
1.10	846	-1.30	-21.49	(+ 0.05 - 0.04)	12.86	(+ 0.66 - 0.52)		0.08	1.02 $\pm$ 0.10	minimal		
1.30	328	-1.30	-22.05	(+ 0.10 - 0.08)	7.42	(+ 1.51 - 1.84)		0.07	0.99 $\pm$ 0.25	minimal		
0.30	306	-1.30	-20.55	(+ 0.23 - 0.22)	16.48	(+ 1.60 - 1.81)		0.18	0.55 $\pm$ 0.16	average		
0.50	440	-1.30	-20.73	(+ 0.11 - 0.10)	22.56	(+ 1.17 - 1.24)		0.16	0.89 $\pm$ 0.18	average		
0.70	372	-1.30	-21.43	(+ 0.11 - 0.13)	12.08	(+ 0.81 - 0.76)		0.15	0.91 $\pm$ 0.18	average		
0.90	1605	-1.30	-21.34	(+ 0.02 - 0.01)	16.97	(+ 0.26 - 0.23)		0.08	1.18 $\pm$ 0.09	average		
1.10	846	-1.30	-21.43	(+ 0.04 - 0.05)	15.40	(+ 0.78 - 1.09)		0.08	1.16 $\pm$ 0.12	average		
1.30	328	-1.30	-22.01	(+ 0.10 - 0.11)	8.70	(+ 1.83 - 2.40)		0.07	1.12 $\pm$ 0.30	average		

Note. – The meanings of columns are the same as in Table 3.

TABLE 7  
SCHECHTER FUNCTION PARAMETERS FOR VERY BLUE GALAXY SAMPLE

$\langle z \rangle$	$N_{gal}$	$\alpha$	$M_B^*$		$\phi^*$		$\sqrt{Var}$	$j_B$	Weights			
(1)	(2)	(3)	(4)	(5)	(6)	(7)	(8)	(9)	(10)	(11)	(12)	(13)
						$\times 10^{-4}$	Gal Mpc $^{-3}$			$\times 10^8$	$L_\odot$	
0.30	321	-1.30	-19.96	(+ 0.11 - 0.12)	19.84	(+ 1.95 - 2.04)	0.18	0.39 $\pm$ 0.09	minimal			
0.50	372	-1.30	-20.38	(+ 0.12 - 0.11)	18.84	(+ 1.91 - 1.71)	0.16	0.54 $\pm$ 0.12	minimal			
0.70	403	-1.30	-20.63	(+ 0.12 - 0.12)	18.45	(+ 1.58 - 1.71)	0.15	0.67 $\pm$ 0.14	minimal			
0.90	1211	-1.30	-20.84	(+ 0.06 - 0.03)	15.06	(+ 0.82 - 0.65)	0.08	0.66 $\pm$ 0.07	minimal			
1.10	621	-1.30	-20.94	(+ 0.08 - 0.07)	12.35	(+ 0.82 - 1.03)	0.08	0.59 $\pm$ 0.07	minimal			
1.30	670	-1.30	-21.02	(+ 0.04 - 0.05)	21.87	(+ 1.26 - 1.19)	0.07	1.13 $\pm$ 0.12	minimal			
0.30	321	-1.30	-19.79	(+ 0.12 - 0.15)	24.39	(+ 2.28 - 2.25)	0.18	0.41 $\pm$ 0.10	average			
0.50	372	-1.30	-20.22	(+ 0.14 - 0.13)	23.63	(+ 2.18 - 3.03)	0.16	0.59 $\pm$ 0.14	average			
0.70	403	-1.30	-20.51	(+ 0.13 - 0.11)	22.57	(+ 2.36 - 2.08)	0.15	0.73 $\pm$ 0.15	average			
0.90	1211	-1.30	-20.72	(+ 0.04 - 0.05)	19.49	(+ 1.11 - 1.38)	0.08	0.76 $\pm$ 0.08	average			
1.10	621	-1.30	-20.84	(+ 0.07 - 0.08)	16.89	(+ 1.33 - 1.60)	0.08	0.74 $\pm$ 0.10	average			
1.30	670	-1.30	-20.86	(+ 0.05 - 0.04)	38.92	(+ 2.06 - 2.16)	0.07	1.73 $\pm$ 0.17	average			

Note. – The meanings of columns are the same as in Table 3.

## APPENDIX

## A. K-CORRECTIONS

The luminosity functions in this paper use Johnson rest-frame  $B$  and  $U - B$  magnitudes and colors. Since  $B_{Johnson}$  matches observed  $B$ ,  $R$  and  $I$  only at certain redshifts, the transformation into rest-frame quantities requires the calculation of K-corrections (e.g., Oke & Sandage 1962; Hogg et al. 2002). Because of the rather limited number of bands (3 for DEEP2), the use of more robust techniques for the calculation of K-corrections as employed by COMBO-17 (Wolf et al. 2003) or SDSS (Blanton et al. 2003) is not possible. The procedure in this work is similar to that of Gebhardt et al. (2003), who used nearby galaxy SEDs from Kinney et al. (1996) to relate the observed color and magnitude at redshift  $z$  to the rest-frame color and  $B$ -band magnitude.

We started with the 43 Kinney et al. SEDs whose spectra cover the range  $1,100 \text{ \AA} \leq \lambda \leq 10,000 \text{ \AA}$  without gaps, as listed in Table A8. Even though the Kinney et al. spectra are integrated only over a small aperture ( $10'' \times 20''$ ) (in contrast to DEEP2 galaxy magnitudes and colors, which are close to total), this approach was chosen in preference to model spectra because the Kinney et al. data represent *real* spectra. The convolution between filter responses and galaxy SEDs followed Fukugita, Shimasaku & Ichikawa (1995) by resampling filters and spectra to the same dispersion (1  $\text{\AA}$ ), using parabolic and linear interpolations respectively. Still following Fukugita et al. (1995), the curves for Johnson  $U$  and  $B$  filters come from Buser (1978) and Azusienis & Straizys (1969) respectively. The throughput curves for the CFHT  $12k \times 8k$  DEEP2  $BRI$  imaging were calculated by Nick Kaiser, who provided filter transmission curves, CCD quantum efficiency curves, and the telescope response function. Normalized curves for the CFHT filters are shown in Figure A11. Calibration of these convolutions used the model atmosphere of Vega calculated by Kurucz that is distributed with the Bruzual & Charlot (2003) galaxy evolution synthesis package. The conversion between Vega and AB magnitudes (Table 1) simply compared the zero-points between the Vega calibration and that obtained using a flat spectrum in  $F(\nu)$  converted into wavelength space (e.g., Fukugita et al. 1995).

Figure A12 compares synthesized  $U - B$  values for the Kinney et al. galaxies with  $U - B$  values for the same galaxies derived from the *Third Revised Catalog of Galaxies* (de Vaucouleurs et al. 1991, RC3). The latter were calculated using the RC3 raw total  $U - B$  colors, corrected only for Galactic absorption using the Schlegel et al. (1998) extinction values tabulated in the NASA Extragalactic Database<sup>13</sup>. Both sets of measurements are therefore consistent in being corrected for Galactic extinction though not for internal absorption or for a face-on geometry. The agreement is fairly good, even though the RC3 values refer to *total* galaxy colors while the Kinney et al. spectra sample the center only. For the reddest templates, the synthetic spectra overestimate  $U - B$  by  $\sim 0.08$  mag; this difference is in the expected direction of the natural internal color gradient. Overall, the good agreement in Figure A12 suggests that the zero-point of our synthetic  $U - B$  system is accurate to a few hundredths of a magnitude.

Figure A13 shows the calculated K-correction  $K_{RB}$  (which converts  $R$  into  $B_{Johnson}$ ) as a function of synthetic observed  $R - I$  color for different redshift intervals, while Figure A14 shows calculated rest-frame  $U - B$  as a function of synthetic observed  $B - R$  in the same redshift intervals. Similar curves of  $U - B$  as a function of observed  $R - I$  for DEEP2 galaxies, are shown in Figure A15.

In general, relations are tight at redshifts where  $U$  and  $B$  are shifted close to the observed passbands but show more scatter as the match worsens. For redshifts beyond  $\sim 0.7$ , where DEEP2 is focused,  $R - I$  color provides a much better estimate of rest-frame  $U - B$  and  $B$  than  $B - R$ .

Finally, Figure A16 compares synthetic DEEP2  $B - R$  versus  $R - I$  colors from the Kinney et al. (1996) SEDs versus real data, binned by redshift. Observed galaxies are the red and green data points, while synthetic colors from the Kinney et al. templates are the black triangles; only 34 templates (identified in Table A1) are displayed here. A similar diagram using the whole set of 43 templates was used to select the final set. Whenever a template was an outlier compared to the observed galaxy distribution, it was flagged; templates flagged in more than two redshift bins were discarded. Galaxies that were discarded have a “no” in column (4) in Table A1 and are shown as asterisks in Figures A2 through A5.

The good agreement between observed and synthesized colors in Figure A16 suggests that, even though evolution of the template SEDs is being neglected in the present K-corrections, the errors introduced are probably small. A reason for this is that the observed color range of galaxies at all redshifts considered in this work is well covered by the spectral locus of the templates. A possible shortcoming of not using evolving SEDs for the K-correction, i.e., K+e corrections, is that at higher redshifts a portion of galaxies might shift into the wrong color class, as discussed by Wolf et al. (2003) and Bell et al. (2004). This problem is avoided in the present work by dividing galaxies into red and blue classes using the evolving “valley” of color bimodality. This does not prevent galaxies from changing color—indeed, the number of red galaxies may grow as blue galaxies migrate across the valley after star-formation quenching—but it does define classes of galaxies in a way that is independent of color zero-point errors.

Second-order polynomials were used to estimate  $U - B$  and the K-corrections from the observed colors. Custom fits were calculated (at the specific redshift of each observed galaxy) of  $U - B$  and the K-correction versus  $B - R$  and/or  $R - I$ . Rest-frame parameters were obtained by entering the observed colors. The range of estimated colors (and K-corrections) was restricted to that covered by the template spectra, so that observed galaxies with extreme colors were forced to have reasonable rest-frame values. For DEEP2 galaxies, at redshifts where rest-frame  $U - B$  lies between  $B - R$  and  $R - I$ , the K-corrections and rest-frame colors were obtained by interpolating between the  $B - R$  and  $R - I$  derived quantities. Otherwise, the rest-frame quantities were obtained using the closest pair of filters. The

<sup>13</sup> <http://nedwww.ipac.caltech.edu>

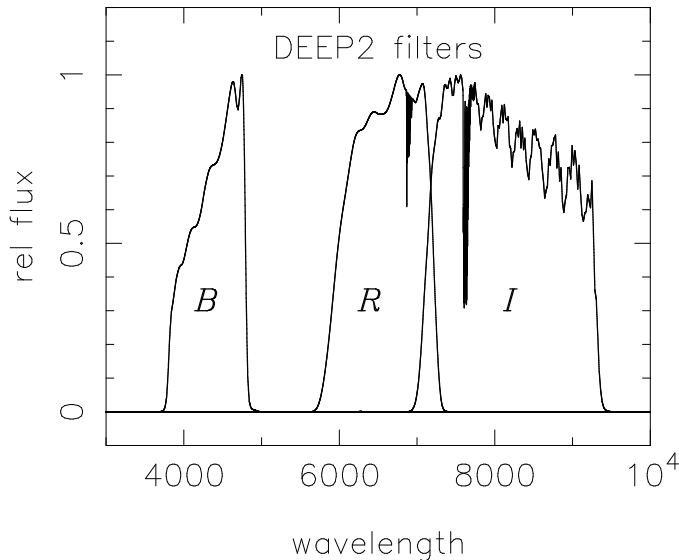


FIG. A11.— Transmission curves of the CFHT  $12K \times 8K$  filter transmission curves (including telescope and CCD throughput) used in DEEP2. Also shown are estimates of the telluric absorption due to the A ( $\sim 6800 \text{ \AA}$ ) and B ( $\sim 7600 \text{ \AA}$ ).

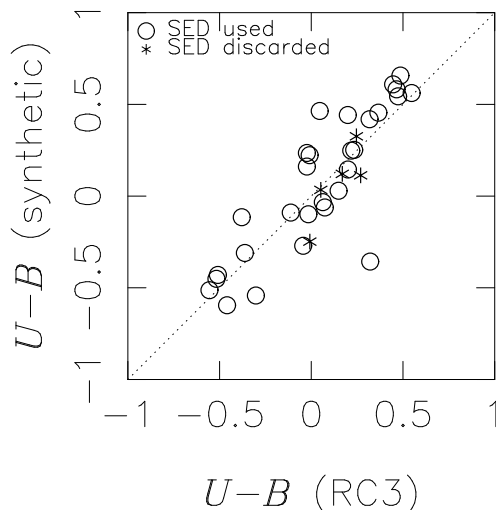


FIG. A12.— Comparison between  $U - B$  colors derived from the RC3, with synthesized  $U - B$  obtained by convolving Johnson filters with the Kinney et al. (1996) spectra. The synthetic  $U - B$  are based on the template SEDs, which are corrected for Galactic absorption only. To match these, the RC3  $U - B$  colors have been corrected for Galactic absorption only (using Schlegel et al. 1998) but not for internal absorption. Galaxies used in the final K-correction fits are shown as circles, while galaxies whose spectra were discarded from the final fits are shown as asterisks. The RC3 measurements are total (containing all the galaxy light), while the Kinney et al. spectra sample only a rectangular  $20'' \times 10''$  box at the center of the galaxy. In spite of this, the deviations from the dotted line are fairly small.

RMS error for estimated  $U - B$  ranges from 0.12 mag at  $z = 1.2$  (worst value) to 0.03 mag at redshifts where the observed filters best overlap  $U - B$ . The RMS error in  $K_{RB}$  ranges from  $\sim 0.01$  mag whenever one of the observed filters overlaps  $B_{Johnson}$  to  $\sim 0.15$  mag at  $z \sim 1.5$ , where a large extrapolation is being used. The results obtained using the parabolic fits are comparable to the results using interpolations between SEDs (Lilly et al. 1995).

This procedure differs from that of Gebhardt et al. (2003) in two ways. First, Gebhardt et al. used nearly all the Kinney et al. (1996) templates after removing only two very deviant spectra. Second, the parabolic fit here between observed and rest-frame parameters is calculated at the exact redshift of each observed galaxy, whereas Gebhardt et al. attempted to calculate a more general polynomial that mapped the color transformation over the entire redshift range.

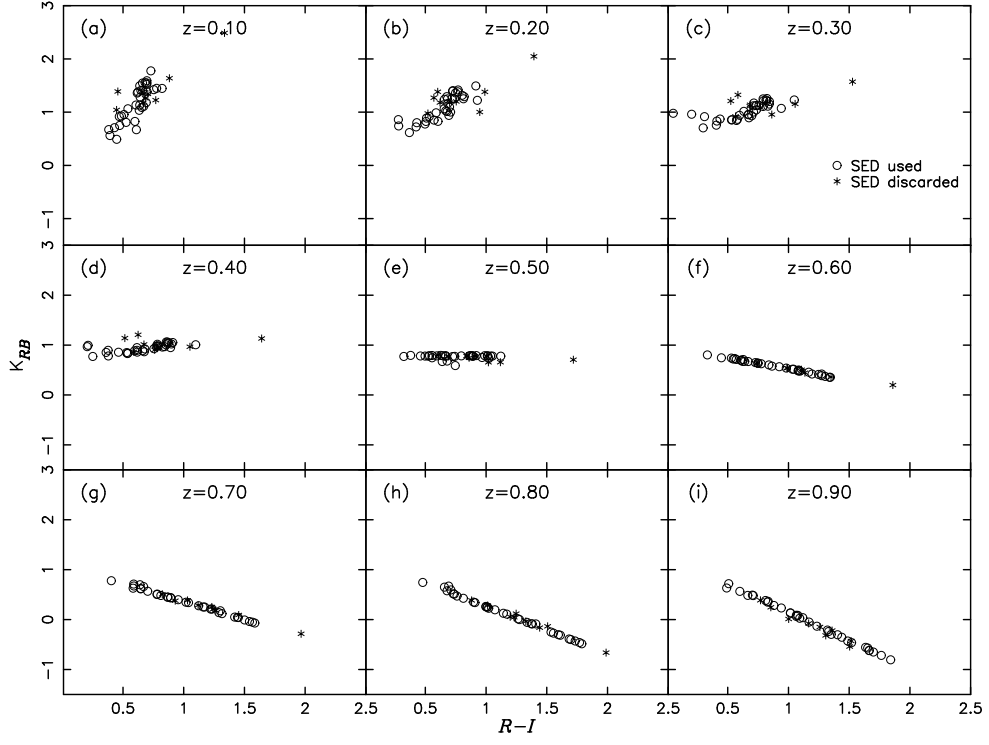


FIG. A13.— The K-correction transforming DEEP2  $R$  to  $B_{Johnson}$  as a function of SED color and redshift  $z$  for all Kinney et al. template galaxies in Table A1. SED color is apparent DEEP2  $R - I$  synthesized from the Kinney et al. (1996) templates at that redshift. Galaxies used in the final fit are shown as open circles, while galaxies removed from the final fit are shown as asterisks. At  $z \sim 0.5$ ,  $R$  and  $B_{Johnson}$  essentially overlap, and there is little dependence of  $K_{RB}$  on observed color.

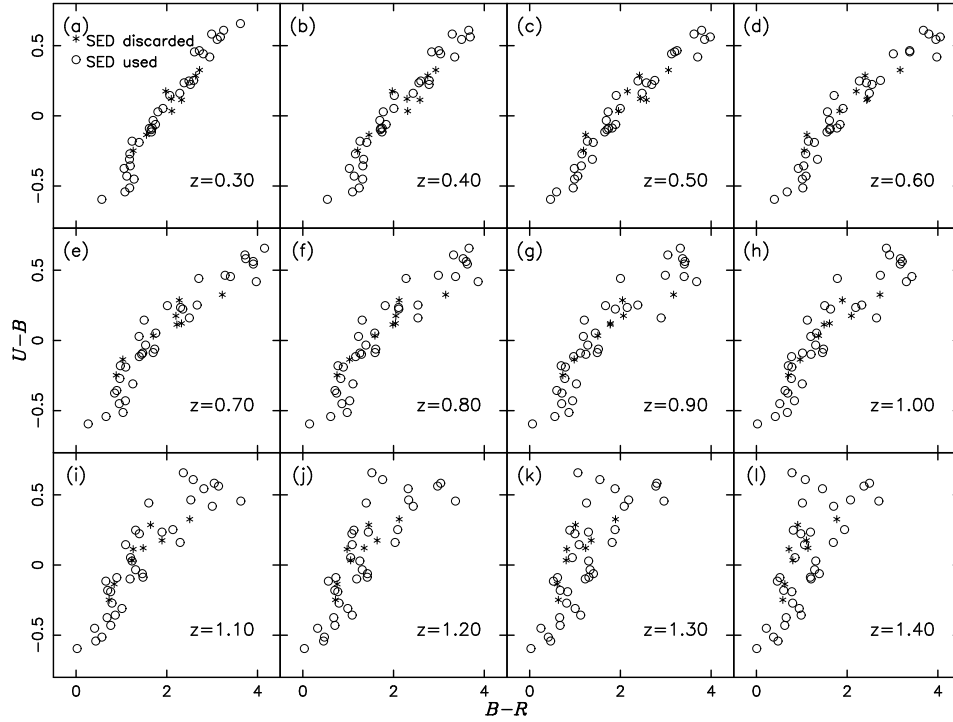


FIG. A14.— Similar to Figure A3, but showing synthesized  $U - B$  color as a function of synthesized observed  $B - R$ , versus redshift for the Kinney et al. SEDs. As the overlap between redshifted  $U - B$  color and observed color decreases towards higher redshifts, the relation becomes noisier.

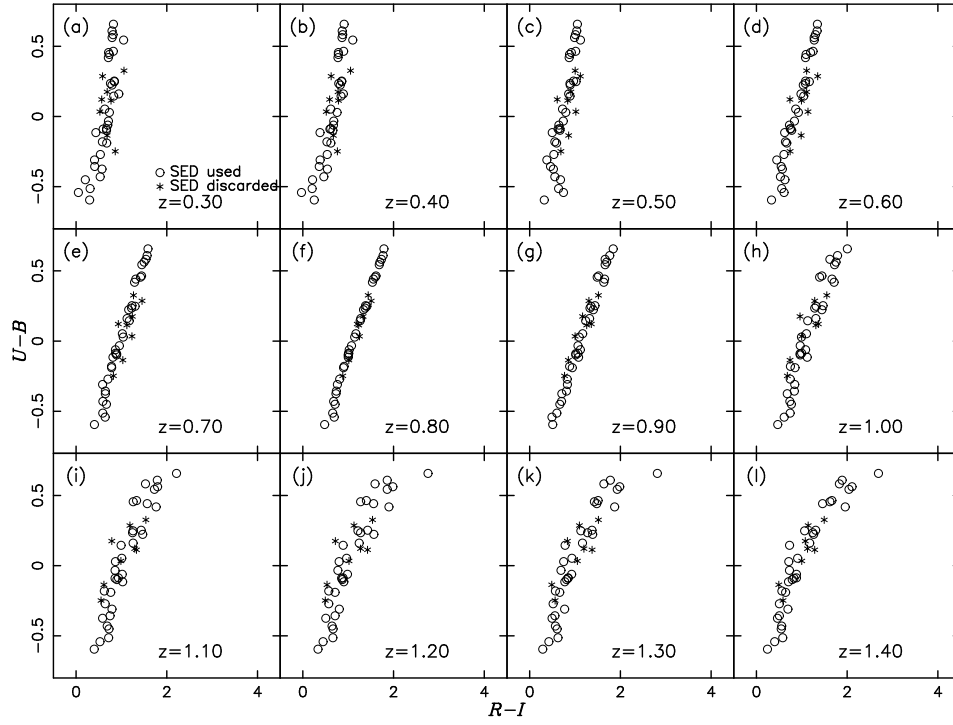


FIG. A15.— Similar to Figure A4, but showing synthesized rest-frame  $U - B$  color as a function of synthesized observed  $R - I$ , used in DEEP2, versus redshift. In contrast to the  $B - R$  plots shown in Figure A4, the relation between  $R - I$  and  $U - B$  gets tighter at high redshift, where  $R - I$  is a better estimator of rest-frame color.

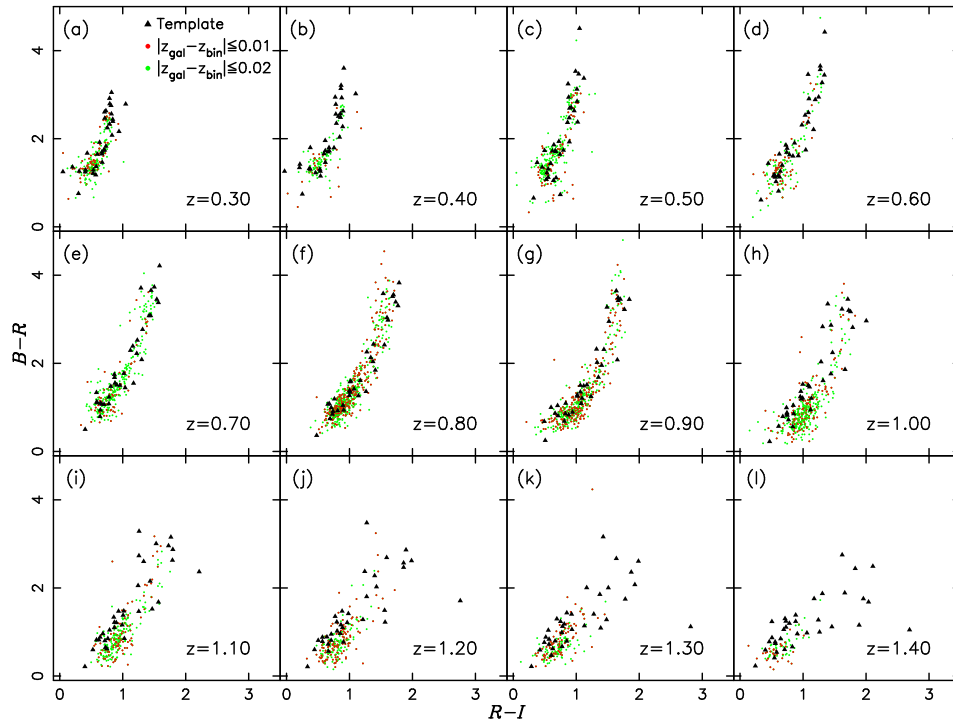


FIG. A16.— Comparison between synthesized  $R - I$  and  $B - R$  colors measured from the final sample of 34 Kinney et al. templates (black triangles) versus observed colors of DEEP2 galaxies. Red dots represent DEEP2 galaxies with good quality redshifts lying within  $\pm 0.01$  of the redshift displayed in the plot, while green dots represent galaxies lying within  $\pm 0.02$  of that redshift. Even though the template SEDs are not evolved, they still provide a good match to the observed data, even at the higher ranges of the sample.



TABLE A8  
KINNEY ET AL. SEDs

Id	$U - B$ (RC3)	$U - B$ (synthetic)	Used in Analysis
NGC 5128	...	0.80	no
NGC 1399	0.49	0.66	yes
NGC 7196	0.45	0.61	yes
NGC 1553	0.47	0.58	yes
NGC 1404	0.55	0.56	yes
NGC 4594	0.47	0.54	yes
NGC 210	0.05	0.46	yes
NGC 1433	0.20	0.44	yes
NGC 1316	0.37	0.46	yes
NGC 2865	0.32	0.42	yes
NGC 1808	0.25	0.33	no
NGC 3393	...	0.29	no
NGC 7582	0.23	0.25	yes
NGC 3081	0.22	0.25	yes
NGC 7083	-0.02	0.24	yes
NGC 7590	-0.01	0.22	yes
NGC 3660	...	0.17	no
NGC 6221	-0.02	0.16	yes
NGC 1097	0.20	0.15	yes
NGC 5102	0.17	0.12	no
NGC 1326	0.27	0.11	no
IC 3639	...	0.05	yes
NGC 1068	0.05	0.03	no
NGC 3351	0.15	0.03	yes
NGC 5135	0.06	-0.03	yes
NGC 7552	0.07	-0.06	yes
NGC 7130	...	-0.09	yes
NGC 7793	-0.11	-0.09	yes
NGC 1672	-0.02	-0.10	yes
NGC 7673	-0.38	-0.12	yes
NGC 4748	...	-0.14	no
CGCG 038-052	...	-0.18	yes
NGC 7496	...	-0.19	yes
NGC 4385	-0.01	-0.25	no
M 83	-0.04	-0.27	yes
NGC 1313	-0.36	-0.31	yes
ESO 296 G 11	0.32	-0.36	yes
NGC 3049	...	-0.38	yes
NGC 7714	-0.51	-0.43	yes
Tololo 1924-416	-0.52	-0.45	yes
NGC 3125	-0.56	-0.51	yes
NGC 5253	-0.30	-0.54	yes
NGC 1705	-0.46	-0.60	yes

Note. – SEDs of galaxies that are used in the calculation of K-corrections are denoted by “yes” in column 4. Galaxies that were discarded because of deviant behavior in two or more redshift intervals are noted by “no.” These are represented as asterisks in Figure A2 (if RC3 data exist) and in Figures A3 through A6.

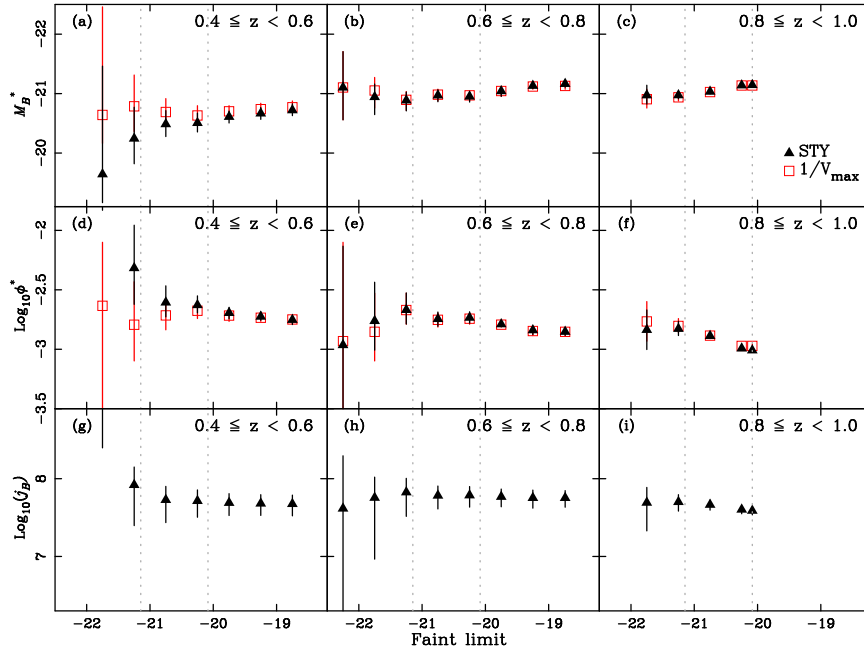


FIG. B17.— Stability of Schechter parameters for red galaxies from DEEP2 as a function of the adopted faint magnitude limit used in the fit. This is calculated in three different redshift ranges, where for each we have limited the data at progressively brighter magnitudes. The vertical grey lines present the actual limits of the data in bins  $z=0.8-1.0$  (right line) and  $z=1.0-1.2$  (left line). Solid black triangles represent fits using the STY method, and open red squares the  $1/V_{max}$  fits. Panels *a-c* show results for  $M_B^*$ , *d-f* results for  $\phi^*$ , and *g-i* results for the integrated luminosity density. All fits use constant  $\alpha = -0.5$ , as in the text. In the lowest-redshift bin, there are very few galaxies brighter than  $-21.5$ , and fits that are highly truncated are poor. Aside from this, the fits are quite stable, indicating that drifts induced by a mismatch in the shape of the Schechter function to the data are small. If anything, the trends here would only *add* to the observed trends. Appendix B provides a more quantitative discussion.

## B. STABILITY OF SCHECHTER PARAMETERS AS A FUNCTION OF FAINT LIMITING MAGNITUDE

A limitation that is invariably present when calculating the luminosity function of galaxies is the smaller domain accessible in absolute magnitudes at higher redshifts. To examine this effect, Schechter fits were re-calculated for DEEP2 red galaxies considering three different lower- $z$  bins and raising the faint limit to brighter magnitudes to match the magnitude ranges accessible in the higher- $z$  bins. Any mismatch in the assumed shape of the luminosity function will result in a spurious drift of the fitted parameters as the magnitude limit is raised. The purpose of this test is to make sure that our measured evolutions in  $M_B^*$  and  $\phi^*$  for red galaxies are not contaminated by this kind of bias.

The results of this test are shown in Figure B17 for red galaxies, where  $\alpha$  has been kept at the value  $-0.5$  used in the main text. Vertical gray lines show the limits of the data in bins  $z=0.8-1.0$  and  $z=1.0-1.2$ . For all three lower bins, we see a drift of  $M_B^*$  of  $\sim 0.1$  mag toward *fainter* values as the samples are truncated, whereas the measured evolution is a *brightening* of  $M_B^*$  back in time. Thus, if anything, the true evolution in  $M_B^*$  is slightly more than claimed. The quantity  $\phi^*$  drifts upward by 0.1-0.15 dex with more truncation whereas the observed effect is a fall back in time, so again, the true evolution may be underestimated. Finally, the important quantity  $j_B$  drifts upward by only 0.05-0.1 dex, confirming its essentially constant nature. A similar study was made for the blue galaxy sample, which shows the same behavior. This test also shows that  $1/V_{max}$  seems to provide a more robust estimate of the Schechter parameters than STY as the domain in absolute magnitudes decreases, though both agree within the estimated errors.

We conclude that errors caused by Schechter function mismatches are in all cases small compared to the measured evolutionary changes for red galaxies.

This figure "f1.jpg" is available in "jpg" format from:

<http://arxiv.org/ps/astro-ph/0506041v3>

This figure "f3.jpg" is available in "jpg" format from:

<http://arxiv.org/ps/astro-ph/0506041v3>

This figure "f4.jpg" is available in "jpg" format from:

<http://arxiv.org/ps/astro-ph/0506041v3>

This figure "f6.jpg" is available in "jpg" format from:

<http://arxiv.org/ps/astro-ph/0506041v3>